

UC Irvine

UC Irvine Electronic Theses and Dissertations

Title

Long and Short Time Scale Mass Capture Mechanisms in Laser Directed Energy Deposition Additive Manufacturing

Permalink

<https://escholarship.org/uc/item/3tc66717>

Author

Haley, James Cameron

Publication Date

2019

Peer reviewed|Thesis/dissertation

University of California,
Irvine

Long and Short Time Scale Mass Capture Mechanisms
in Laser Directed Energy Deposition Additive Manufacturing

Dissertation

submitted in partial satisfaction of the requirements
for the degree of

DOCTOR OF PHILOSOPHY

in Materials Science and Engineering

by

James Cameron Haley

Dissertation Committee:
Professor Enrique J. Lavernia, Chair
Professor Julie M. Schoenung
Professor Lorenzo Valdevit

2019

Figure 18 © 2015 Elsevier
All other materials © 2019 James Cameron Haley

DEDICATION

To

My parents, Dan and Mary Haley.

TABLE OF CONTENTS

	Page
LIST OF FIGURES	iv
LIST OF TABLES	v
ACKNOWLEDGEMENTS	vi
CURRICULUM VITAE	vii
ABSTRACT OF THE DISSERTATION	viii
INTRODUCTION	1
CHAPTER 1: Working Distance Passive Stability in L-DED	8
CHAPTER 2: Observing Particle-Melt Pool Impact Events in L-DED	30
CHAPTER 3: Numerical Modelling of Particle Impact	47
FUTURE WORK	77
SUMMARY AND CONCLUSIONS	79
REFERENCES	80

LIST OF FIGURES

	Page
Figure 1	Optomec LENS® 750 and deposition head 1
Figure 2	Schematic cross section of the melt pool 2
Figure 3	Time and length scales of tool used in analysis of L-DED 4
Figure 4	Graphical Abstract Outlining Chapter 1 8
Figure 5	Powder Spray Pattern and Modelled Gaussian Fit 14
Figure 6	Flow Diagram of Track Dimension Prediction Model 15
Figure 7	Laser Energy Absorption in Powder Cloud 18
Figure 8	Single Track Cross Section Dimension Definitions 21
Figure 9	Model Validation vs. Experimental Measurement 22
Figure 10	Working Distance Effects on Deposition and Stability 25
Figure 11	Thermal Buildup Effects on Stable Working Distance 27
Figure 12	Powder Spray Pattern Effects on Stable Working Distance 28
Figure 13	Schematic of L-DED 31
Figure 14	Characterization of Powder Spray with High Speed Video 38
Figure 15	Video Demonstration of Powder-Melt Pool Interactions 39
Figure 16	Formation Origins for Attached Particles 40
Figure 17	Particle Deflection Off Floating Particles 44
Figure 18	Submergence, Rebound, and Oscillation Regimes of Particle Impact 51
Figure 19	Particle Impact Model Fidelity Hierarchy 62
Figure 20	3D Representation of Particle Impact Model 63
Figure 21	Time Series of Particle Impact Model 63
Figure 22	Heat Accumulation in Particle Over Time 64
Figure 23	Influencing Factors on Particle Residence Time 66
Figure 24	Comparison of Analytical and Numerical Models 69
Figure 25	Conduction Vs Radiation Scaling Behavior of Particle Residence Time 71
Figure 26	Particle Wettability Influence on Impact Regime 72
Figure 27	Estimating Particle Contact Angle 74

LIST OF TABLES

		Page
Table 1	Composition of Stainless Steel 316L Powder	12
Table 2	Machine Parameters for Single Track Validation Matrix	12
Table 3	Physical & Experimental Constants and Machine Parameters	15
Table 4	Terms and Symbols	24
Table 5	Codes for Equipment in High Speed Video Setups	35
Table 6	Sample Captured Video and Setup Parameters	36
Table 7	Design of Experiment Levels for Numerical Models	56
Table 8	Hierarchy of Model Fidelities	57
Table 9	Temperature Dependent Stainless Steel 316L Properties	57
Table 10	Temperature Independent Stainless Steel 316L Properties	58
Table 11	Other 316L Thermophysical Properties	58

ACKNOWLEDGEMENTS

I would like to express my deepest gratitude and respect for my advisor, Professor and Provost Enrique J. Lavernia. His unyielding commitment to provide the time, facilities, and funding has made this work possible. He is a living testament that the conventionally perceived limits of human ability are no match for intelligent, targeted planning and efficient allocation of effort. Extraordinary appreciation is also owed to my co-advisor, Professor Julie M. Schoenung. Your guidance is always well-considered, your insight always clear, and your support always steadfast. Few of my choices in life so far have paid out half so well as the decision to trust both of you. Thank you.

I also owe Darryl Mack so much for making all the lab's ideas real. I have learned so much from our conversations and your work; I knew from the beginning I'd never be able to pay it back, so I'm settling by trying to pay it forward. I strongly suspect that's a tally that even the first students you mentored are still struggling to match.

It truly takes a tribe to raise a PhD, and my labmates and co-workers have been one of the most supportive and well-coordinated groups of individuals I have ever encountered. I cannot even begin to thank you all enough for your time and companionship. Stay in touch!

Outside of the UCI team, the interest, support and guidance of Nancy Yang and Josh Yee at Sandia National Labs have been instrumental in this work. I've also greatly benefited from the help of Larry Vladic from Elite Motion Systems, Mark Doerfler from Vision Research, and Todd Rumbaugh from Hadland Imaging for providing the opportunity to utilize the incredible video equipment used in these investigations. This work was supported financially by Sandia National Laboratories [1687547] as well as from the Army Research Office [Grant W911NF1810279]. Thank you to Elsevier for permission in reprinting prior publications in this dissertation.

CURRICULUM VITAE

James Haley

Education and Work Experience

- 2008-12 B.S. in Ceramic and Materials Engineering, Clemson University
- 2012-14 Steel Business Associate at TimkenSteel, Canton, OH
- 2014-15 M.S. in Chemical Engineering and Materials Science,
University of California, Davis
- 2016-18 PhD in Materials Science and Engineering,
University of California, Irvine

Publications

- J.C. Haley, J. M. Schoenung, and E. J. Lavernia, “Numerical and Analytical Analysis of Particles Impacting and Floating on the Melt Pool Surface in Laser Directed Energy Deposition (LDED),” In Preparation.
- J.C. Haley, B. Zheng, U.S. Bertoli, A.D. Dupuy, J.M. Schoenung, E.J. Lavernia, Working distance passive stability in laser directed energy deposition additive manufacturing, *Materials & Design*. 161 (2019) 86–94. doi:[10.1016/j.matdes.2018.11.021](https://doi.org/10.1016/j.matdes.2018.11.021).
- J.C. Haley, J.M. Schoenung, E.J. Lavernia, Observations of particle-melt pool impact events in directed energy deposition, *Additive Manufacturing*. 22 (2018) 368–374. doi:[10.1016/j.addma.2018.04.028](https://doi.org/10.1016/j.addma.2018.04.028).
- K.L. Terrassa, J.C. Haley, B.E. MacDonald, J.M. Schoenung, Reuse of powder feedstock for directed energy deposition, *Powder Technology*. 338 (2018) 819–829. doi:[10.1016/j.powtec.2018.07.065](https://doi.org/10.1016/j.powtec.2018.07.065).
- Y. Sun, J.C. Haley, K. Kulkarni, M. Aindow, E.J. Lavernia, Influence of electric current on microstructure evolution in Ti/Al and Ti/TiAl3 during spark plasma sintering, *Journal of Alloys and Compounds*. 648 (2015) 1097–1103. doi:[10.1016/j.jallcom.2015.07.079](https://doi.org/10.1016/j.jallcom.2015.07.079).

ABSTRACT OF THE DISSERTATION

Long and Short Time Scale Mass Capture Mechanisms
in Laser Directed Energy Deposition Additive Manufacturing

By James Cameron Haley

Doctor of Philosophy in Materials Science and Engineering

University of California, Irvine, 2019

Professor Enrique J. Lavernia, Chair

Laser Directed Energy Deposition (L-DED) Additive Manufacturing (AM) offers unprecedented flexibility in direct fabrication of metallic components in a way that can be readily integrated with existing CNC subtractive machining technologies. The core building block of the technology is the melt pool, the dynamic bead of molten material established by the energy equilibrium between incident laser energy and thermal dissipation. While the unique solidification microstructure of the melt pool has attracted intense scrutiny, the mechanisms determining how mass is originally incorporated into the melt pool have been less well studied. In this work, three new tools are applied to the task of broadening the understanding of mass capture behavior. First, over long time scales it was observed that mass capture efficiency evolves over the course of depositing many layers as machine conditions change; a non-empirical model constructed to track this revealed self-stabilizing behavior in working distance in open-loop control systems. Second, on very short time scales, high speed videography was employed to understand what happens at the moment of impact between a feedstock powder particle and the melt pool. It was revealed that particles are captured by surface tension before fully melting. Third, this particle retention time was investigated with numerical simulation to highlight its relationship to particle size, impact velocity, thermal distributions and wettability.

INTRODUCTION

The Laser Directed Energy Deposition (L-DED) Process

The Laser Directed Energy Deposition (L-DED) process is the focus of a fast expanding pool of experimental and modeling research, spurred on by the advantages of geometric flexibility and low lead time that the process offers over conventional manufacturing practices [1], [2]. In L-DED, a laser is focused on a substrate, melting a small pool of metal into which feedstock powder is sprayed, adding mass and building the pool in size. The substrate is then rastered in the X-Y plane to shape the added material to a cross section of the preprogrammed geometry; the laser and nozzle assembly are moved up in the Z direction at a fixed increment, and the process is repeated for the next cross section. Figure 1 depicts the overall and key components of the Optomec LENS® 750 machine used in this work.

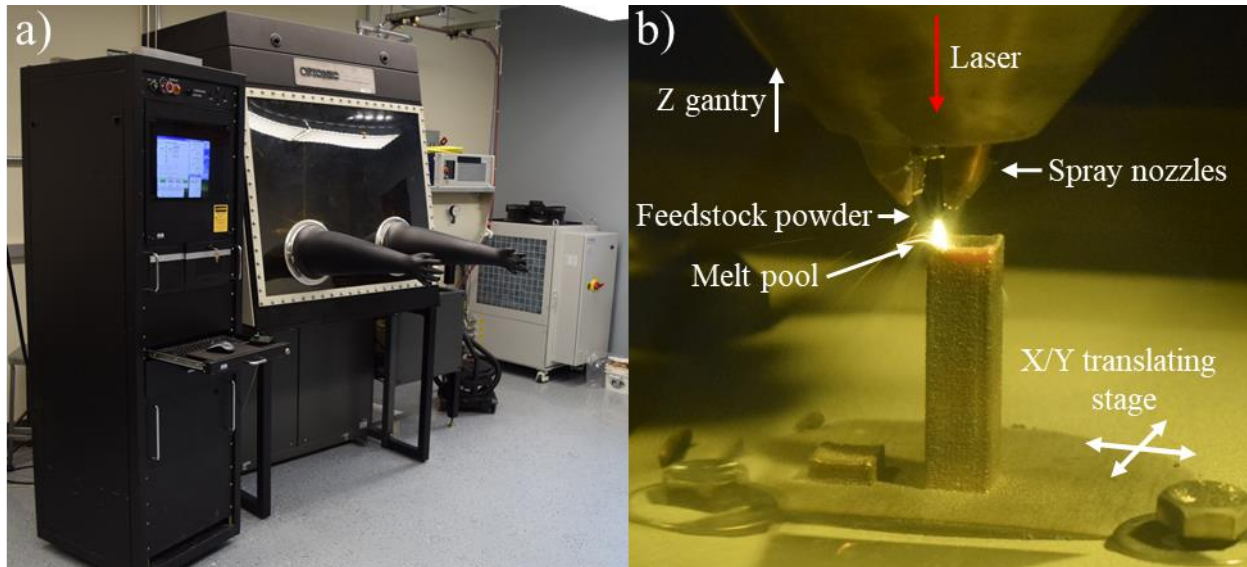


Figure 1. a) Optomec LENS® 750 system used for all L-DED studies. In b), key components of the L-DED process are identified.

The melt pool generated by the laser is the building block of the overall deposited part, as diagrammed in Figure 2, and its morphology is a function of many physical interactions, including:

- An energy equilibrium between incident laser energy and heat dissipated through conduction and convection through the melt pool and the base substrate material [3]
- Surface tension gradients generated from the thermal field that causes Marangoni convection, dependent on surface active elements [4]–[6]
- The ‘keyholing’ phenomenon, where vaporization from high laser intensity causes back pressure and forms a cavity that penetrates deeply into the base material. The walls of this cavity can collapse, bridge over, and solidify leaving behind porosity [7]–[9]
- The carrier gas flow rate and powder-melt impact events which stochastically disrupt the surface tension driven liquid surface [10], [11]

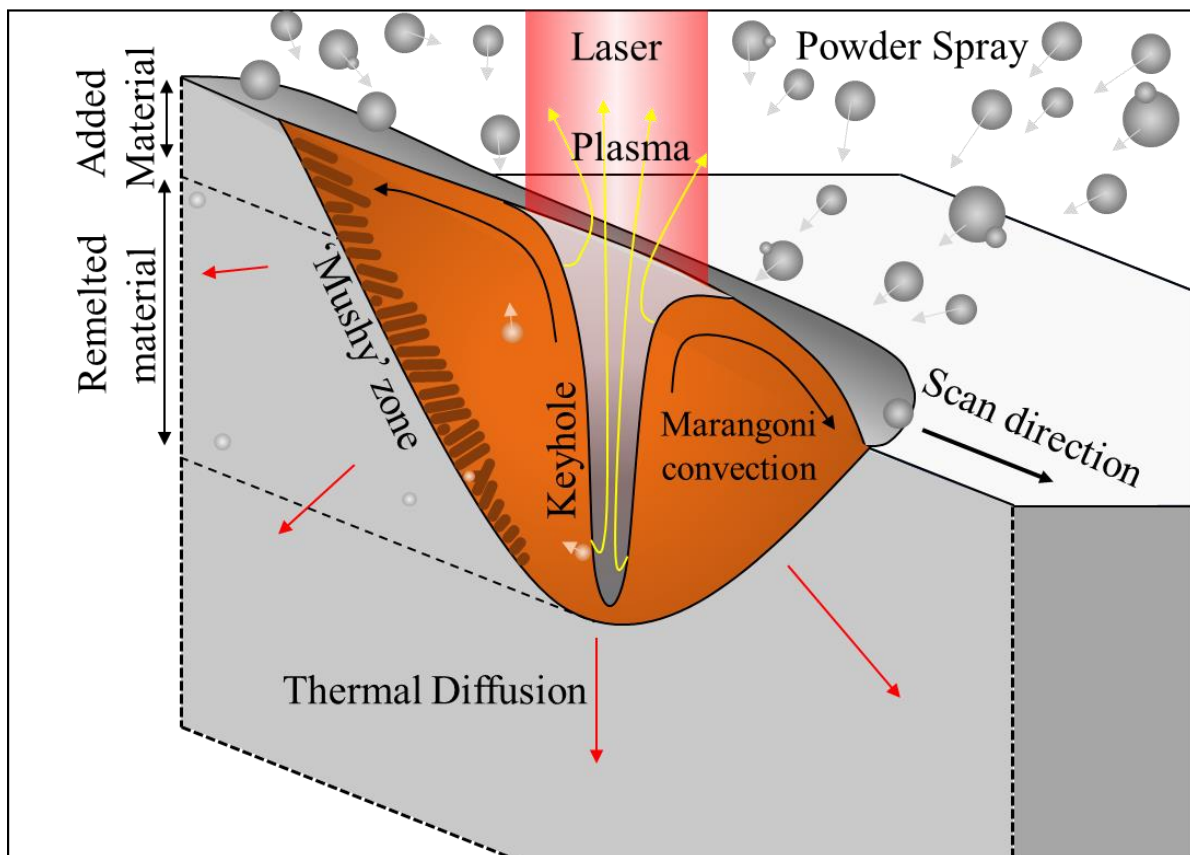


Figure 2. Schematic cross section of the melt pool, as a function of energy and mass equilibria. Incident laser energy generates a convecting melt pool, which is quenched by thermal diffusion through supporting material, radiation from free surfaces, and occasionally evaporation of metal. Mass is delivered through sprayed powder feedstock, which melts into the melt pool before finally solidifying as the laser moves on.

Scaling constraints of tools used to study L-DED

Understanding these physical interactions occurring around the melt pool is critical to effective control of the process and microstructure. Numerous experimental and modelling tools have been applied to L-DED and other laser melt techniques, such as in-situ thermal imaging[12], high speed video [13], [14], spatial, optical, and pyrometric measurement systems [15]–[17], as well as thermal and residual stress models [18]–[20], melt pool convection and thermal models [5], [9], [21], powder spray models [22], and solidification models [23], [24], to name but a few. However, these physical interactions in L-DED occur over highly different time and length scales, which becomes a serious challenge when developing monitoring or modelling techniques. This dilemma is illustrated in Figure 3. For instance, a deposited part can be up to hundreds of millimeters in size, deposited over the course of hours, while the melt pool is less than a millimeter which moves at tens of millimeters per second. If one developed a CFD model or an in-situ thermal camera to measure the melt pool characteristics, the required execution time or stored data would not scale reasonably to allow measurement for an entire part. This scaling problem becomes even worse when one considers that the feedstock material is a powder, and individual powder particles are typically 5-100 μm in size, and moving quickly, on the order of meters per second.

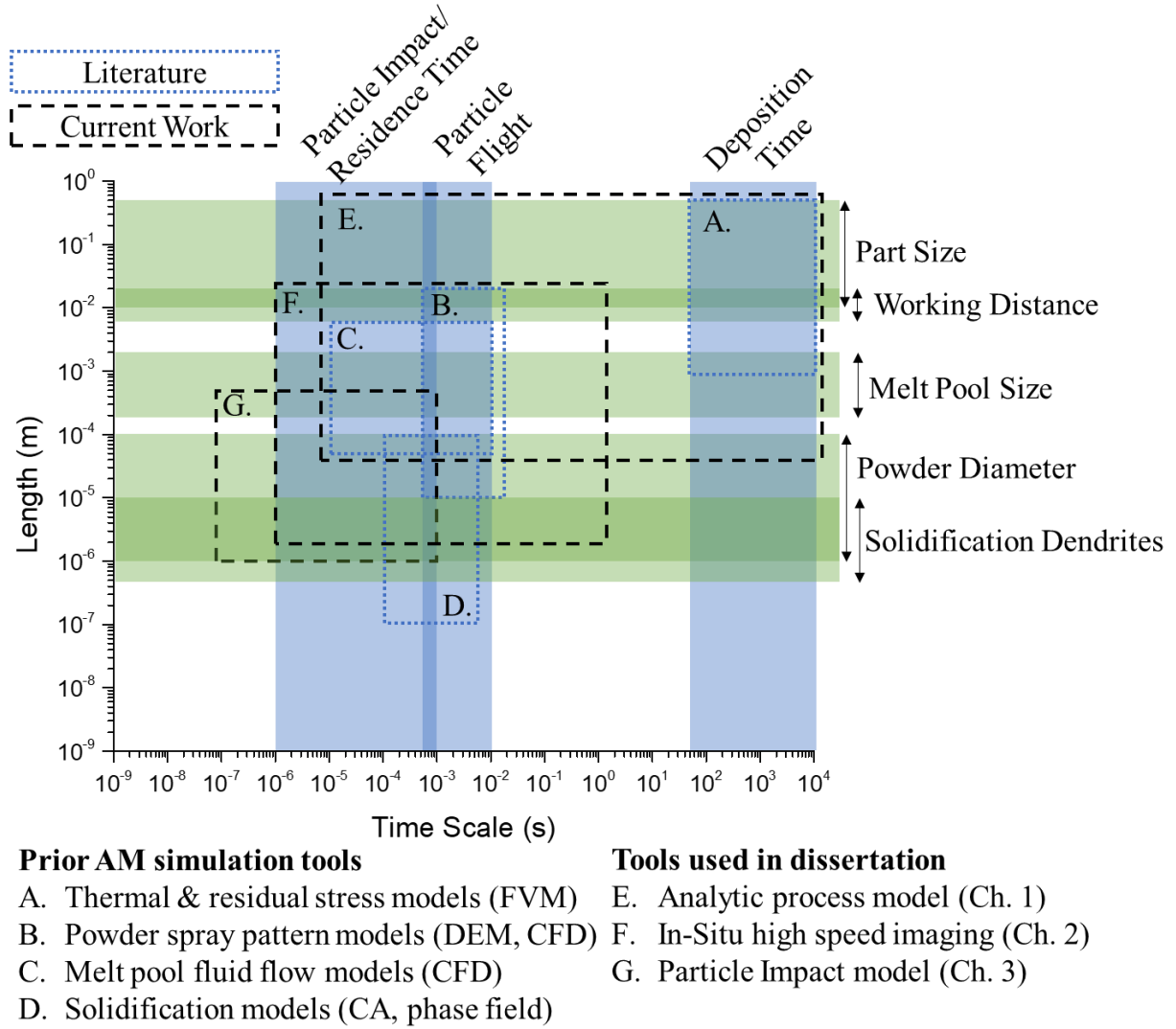


Figure 3. Length and time scales of various phenomena occurring in L-DED, compared to the orders of magnitude of the capability of various tools applied to the system.

Every tool and model applied to better understand L-DED has a natural time and length scale at which it works best. This can artificially constrain investigation to the scales of the measurement technique, not the process itself. The following chapters are unified by the theme of extending existing tools to examine the gaps that have been largely overlooked, as shown in Figure 3: in Chapter 1 a hierarchical process model is used to link part-scale and melt pool-scale interactions, in Chapter 2 high speed video was applied to push to smaller time and length scales

to understand particle-melt pool impact interactions, and in Chapter 3 these impact events are studied at even smaller scales by constructing a Finite Volume Method model.

Mass Capture Efficiency and Motivated Studies

The microstructural formation in laser melting techniques all fundamentally depend on the complicated thermal and mass transport inside the melt pool. This has been extensively studied with creative in-situ monitoring [15] and numerical CFD studies [18]. However, while L-DED, SLM, laser cladding, and laser welding can be fairly analogous in terms of solidification, one unique feature of L-DED is that powder is sprayed, and the melt pool is small relative to the spray pattern. This results in only a portion of the sprayed powder actually landing in the melt pool, which can be expressed with the metric defined here as ‘mass capture efficiency’, the ratio of mass deposited to the powder mass sprayed. Relying on spraying feedstock material as a mass source for L-DED causes the process to behave in several fundamentally different ways than in SLM. Consider that:

- The relative position of the melt pool in the powder spray pattern will alter the number of particle trajectories intersecting the melt pool, and therefore the mass capture efficiency.
- Mass added to the melt pool from the sprayed powder will alter its shape and introduce another heat sink, and therefore alter the thermal gradients and solidification patterns.
- The laser will interact with both powder in flight and the melt pool surface.
- Feedstock powder enters the melt pool primarily from the top surface of the pool, instead of from its leading edge.

With these differences in mind, it becomes clear that many of the excellent studies performed in SLM are not able to address the issues that arise from a sprayed powder feedstock.

Two fundamental questions are left unanswered that drive the entirety of the work contained in this dissertation:

1. How can unique features of L-DED such as the powder spray pattern and melt pool morphology influence the mass capture efficiency, and how does a non-constant mass capture efficiency affect the L-DED process?
2. What happens at the precise moment when mass is introduced to the melt pool, when a powder particle impacts the top surface of the molten metal?

These two questions demand a more fundamental understanding of the transfer mechanisms surrounding mass capture efficiency. In Chapter 1, it was observed that minor errors between actual and predicted layer heights do not accumulate under some process conditions for open loop control systems. A hypothesis was posed that some self-stabilizing effect was being generated. Previous literature has recognized that accumulation of heat in the deposition will alter melt pool size and microstructure [25]. This raises the question of if there may be other long-term interactions between local equilibrium of the melt pool and the global form of the deposited part that could alter the self-stabilizing effect. To understand this local-global interaction, a MATLAB model was constructed that incorporates predictions across several of the physical domains of L-DED, including powder spray pattern, laser attenuation, melt pool local thermal equilibrium, and global mass accumulation. A new phenomenon was observed from the constructed model, where the working distance (also known as stand-off distance) depends strongly on the shape of the powder spray pattern and over the course of many layers, self-stabilize. While this passive stability phenomenon that depends on mass capture efficiency has been qualitatively recognized before, the work laid out here represents the first quantitative, mechanistic explanation in the AM literature.

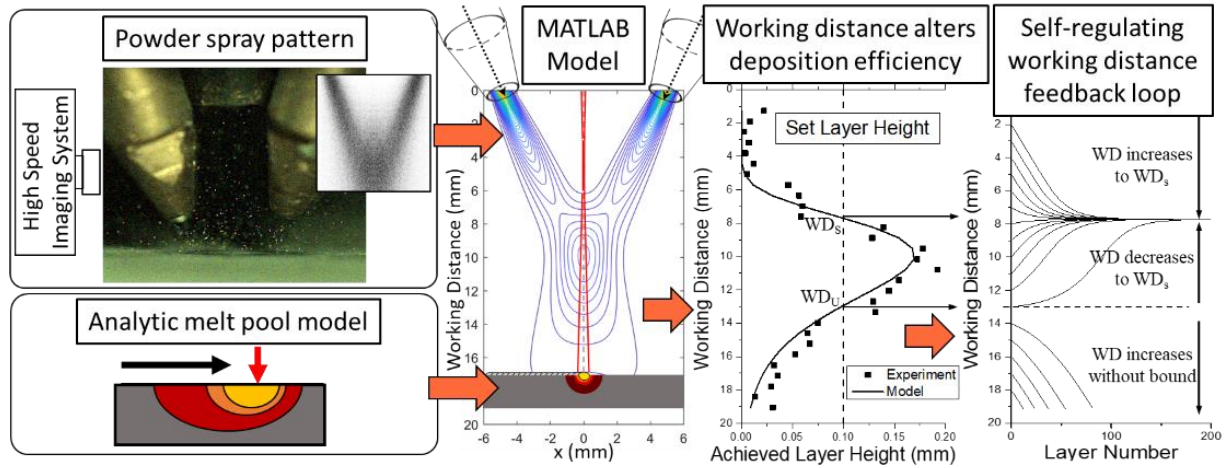
Mass capture efficiency was shown to depend on global trends in L-DED, but this representation assumes all powder particles intersecting the melt pool are incorporated into the melt pool and does not mechanistically describe how mass and heat transfer happen when an individual powder particle interfaces with the fluid of the melt. In the second chapter, the experimental technique of high speed video is used to uncover what precisely happens in the microseconds surrounding the moment of interaction between an incoming powder particle and the surface of the melt pool. This is inspired from recent publications in the powder bed SLM literature that highlighted the fact that evaporating metal from the melt pool strongly displaces and scatters powder from its nominally static position [14]. In L-DED, which have significantly larger particle and melt pool sizes, a different behavioral regime was observed where particles will become trapped by surface tension and float for a brief period of tens to thousands of microseconds before fully melting. This can contribute to loss in mass capture efficiency, as floating particles will shield and saturate the surface of the melt pool and deflect further incoming particles.

While high speed video allowed discovery of the mechanism for capture of individual powder particles, the dependence of this mechanism on process conditions was still unknown. In the third chapter, the particle impact and floatation were numerically modeled to quantify the influences of variables such as melt pool superheat, particle size, and wettability. A Finite Volume Method (FVM) model was constructed in the commercial software COMSOL® Multiphysics that tracks three phase fields (solid, liquid, and gas), surface tension, laminar fluid flow, thermal conduction and convection. The model also implements a custom phase conversion equation that couples the thermal field to the phase field simulating the melting process. The model successfully represents particle capture, and the trends from numerical findings are compared to a simplified one-dimensional analytic representation of thermal dissipation around a powder particle.

CHAPTER ONE: WORKING DISTANCE PASSIVE STABILITY IN LASER DIRECTED ENERGY DEPOSITION ADDITIVE MANUFACTURING

Published in *Materials and Design*, Jan 5th 2019

Figure 4. Graphical Abstract



Abstract

In Laser Directed Energy Deposition (L-DED), closed loop control systems can be used to enhance system reliability; however, modulating controlled parameters can have unintended secondary morphological and microstructural effects. To enable development of control systems more sensitive to the complicated interplay between powder flow, thermal transfer, and long term stability in the machine, the L-DED process, in an open loop configuration, was studied both experimentally and theoretically. A fully physics based semi-analytical model was created that incorporates descriptions of the powder spray pattern, laser attenuation through the powder cloud, and a thermal equilibrium model to predict melt dimensions. The model was validated against an experimental matrix of 258 single track deposition experiments. It was found that the powder flow field causes working distance (WD) to converge to an equilibrium value, and that this equilibrium position is strongly influenced by many effects, such as thermal energy accumulation in the part

and powder flow dispersion. Several metrics to quantify the stability of this equilibrium working distance are proposed and discussed.

1. Introduction

In order to robustly control such a complicated system, process dynamics must be understood and mapped in a way that is able to extend across a vast number of powder, material, laser, and geometric parameters. While a variety of real-time closed loop control methods have been shown to improve machine capabilities and geometric control [15], [26], these ‘active’ systems do not totally circumvent the necessity of understanding the process to control it. For instance, intentionally modulating a parameter, such as scan speed, to control geometry can have additional microstructural consequences, such as altering the solidification rate and grain size [27]. In contrast to this approach, some limited research has been performed on investigating and enhancing ‘passive’ stability phenomena, where an open loop system is able to maintain a desired condition, such as constant working distance (WD) [28], through architecting process conditions to provide a self-regulating feedback loop [29]. For instance, success in passively controlling working distance drift has been reported through taking advantage of the fact that changes in working distance will affect laser focus, which changes laser spot size and can modulate mass capture efficiency [30]. However, this is only claimed to work specifically for a subset of materials that have an increase in surface tension with temperature, so that convective patterns contain the pool within the laser spot. This raises an important question: what other existing or potential feedback loops can stabilize or destabilize a build that arise from the complicated physics at play?

To address the problem of how process conditions may result in a stabilizing feedback loop, several tools are considered. On the experimental side, parametric experimental sweeps of a simplified geometry coupled with metallurgical analysis is a frequently used and straightforward

way to isolate machine conditions [31]–[33] and develop operational heuristics [34]. Additionally, in-situ monitoring can be used to track melt pool geometries, temperatures, and powder spray patterns, which can be related to obtained deposit properties. On the theoretical side, with appropriate assumptions components of the L-DED system can be represented analytically; a popular example being the Rosenthal thermal model of a moving point heat source across a semi-infinite plane [35] which was originally developed for welding but has been used to great effect in L-DED [3], [36], [37]. Numerical techniques such as the Finite Volume Method (FVM) can be used to reduce the necessary assumptions required by analytic models and combine multiple physical processes simultaneously at the cost of computational expense. As reviewed by Pinkerton [18], these tend to fall into three categories based on the domain modelled: the powder flow streams [22]; the melting, flow and solidification at the laser-substrate interaction volume; or the thermal history of the overall part as it is built [19], [38], [39]. This partitioning exists because of the practical computational challenge of spanning the different time and length scales involved for each domain. While numerical methods have led to greater understanding of these isolated domains, this computational limitation limits their use in the current problem of studying feedback loops that depend on all of these domains over the course of many layers.

In the present study, the instabilities that can develop during deposition due to heat buildup and working distance changes due to an evolving melt pool shape are investigated through constructing a system of physics-based analytic equations that account for powder flow, laser attenuation, and melt pool geometry. This model avoids fitting model predictions with coefficients which treat the process as a ‘black box’ that can obscure process relationships. It is demonstrated that a passively stable working distance is generated entirely by the morphology of the powder spray pattern, and that this stability point evolves as a function of the temperature rise due to the

accumulation of thermal energy in the built part. The model is compared to experimental data, and the implications of this model on reliability and control of L-DED are discussed.

2. Materials and Methods

2.1 Single track experiments

258 single tracks deposited under unique processing conditions were used to provide a baseline validation for the model. The system used was a LENS® 750 (Optomec, Albuquerque, NM) fitted with a 1000 W continuous wave IPG Photonics YLR fiber laser. The laser was measured to have a beam quality factor M^2 of 24.7 and a central wavelength of 1070 nm; it was focused with a fused silica lens with a 150 mm focal length at 1064 nm. The laser waist was adjusted to be 10.8 mm above the substrate, for an approximate spot diameter of 0.84 mm.

The powder was gas atomized 316L stainless steel (Carpenter Powder Products, Pittsburgh, PA), that was specified to have a particle size range of 45-106 μm . Composition analysis of the powders was obtained by EAG Laboratories in Liverpool, NY, through three techniques: Instrumental Gas Analysis, Inductively Coupled Plasma Optical Emission Spectroscopy, and Glow Discharge Mass Spectroscopy, and is presented in Table 1. 3/16" thick substrates of 304L stainless steel were used in the cold rolled condition and sandblasted for uniform surface finish. Powder feed rate (F) was set to three different levels: 7.1, 14.1, and 28.1 g/min, fluidized in an argon flow stream of 3.78 L/min, and blown through four 1.12 mm inner diameter nozzles angled at 25° off of the laser axis, with a projected convergence at 10.7 mm working distance from the bottom of the nozzles. Argon shield gas used to protect optics from hot rebounding powder was flowed at a rate of 20 L/min through the central throat.

Table 1. Weight percent chemical composition of 316L stainless steel powder used.

Fe	Cr	Ni	Mo	Mn	Si	N	C	P	O	S
66.20	17.4	12.6	2.24	0.860	0.670	0.099	0.016	0.011	0.018	0.0037

Nine different laser power levels (P) and twelve traverse speeds (S) were used as outlined in Table 2. Tracks that did not adhere to the substrate were discarded. Tracks that showed excessive vapor plume generation were halted and higher powers not executed to protect optics. All of the deposition experiments were performed in argon at lower than 20 ppm oxygen concentrations.

In addition to this matrix, an independent parameter sweep that varied working distance was performed to validate the model's response to adjusting the position of the powder spray nozzles. S, P, and F were kept constant at 16.9 mm/min, 305W and 17 g/min. This portion of the study also held the laser focus at a constant height above the substrate to isolate effects from spray nozzle position.

Table 2. Machine parameters for single track validation experiments.

	Design 1: Full factorial expansion*	Design 2: Single parameter sweep	
Parameter	Levels	Values	Unit
Traverse Speed (S)	6.35-29.6 in 2.12 incr.	16.9	mm/s
Laser Power (P)	75, 126, 176, 227, 277, 328, 378, 429, 479, 530	328	W
Powder Feed Rate (F)	7, 14, 28	25	g/min
Working Distance (WD)	7.49	1.27-19.1 in 0.635 incr.	mm
Results presented in:	Figure 9	Figure 10	
* Combinations producing excessive material evaporation removed to prevent machine damage.			
*Combinations producing no deposition are not included in presented results.			

2.2 Powder flow distribution calibration

To calibrate powder flow, high speed video of powder in flight was recorded at 10,000 frames per second (FPS) with an iX iSpeed 720 camera with a Cavitar CAVILUX Smart illumination laser and a K2 Infinity Distamax long distance microscope provided by Hadland Imaging in Santa Cruz, CA. A single 100 ns, 50 mJ pulse of light was delivered each frame at a

wavelength of 638 nm. Fluidizing and shield gas flow rates were the same as used for single track experiments, but with a powder mass flow rate of 29.6 g/min. The long-distance microscope ensured narrow depth of field of approximately one millimeter, which provides a narrow near-2D ‘slice’ of the powder concentration field in plane with two of the four nozzles’ powder spray axes. One second was recorded and image analysis software was used to count locations of over one million particles, providing a large statistical data source for particle concentration distribution. Count distributions perpendicular to the nozzle axis were calculated and fit with Gaussian profiles and the extracted standard deviations plotted against distance along the nozzle axis in Figure 5. The modeled 3D function for powder concentration as described in the following calculation section is visible as black contours.

A second video at 30,000 FPS was recorded of one nozzle only with similar illumination and higher magnification to measure particle velocities. Fifty particle trajectories were manually tracked over four frames each. For the flow conditions stated the measured average velocity was 7.0 m/s. The powder loading of 29.6 g/min at this flow rate was low enough that few particle-particle interactions were observed just outside the nozzle; therefore, it is assumed assumption that powder trajectories depend primarily on gas flow and nozzle design, and altering feed rate only scales the concentration distribution without affecting its distribution.

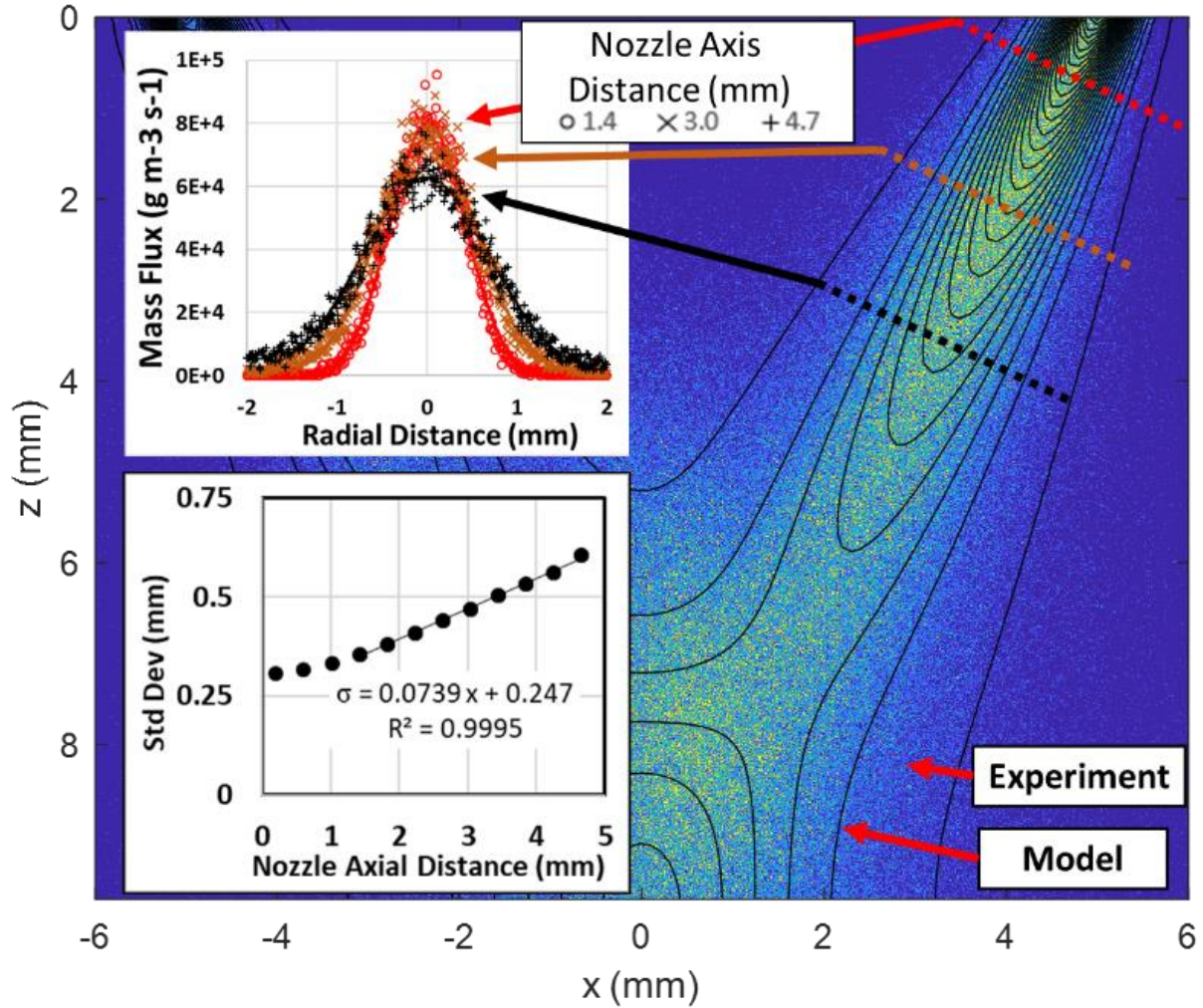


Figure 5. Experimental (color) and modelled (contours) powder concentrations from four spray nozzles, as recorded by high speed video for over one million particles. As seen in the top left inset, flow was found to be Gaussian sufficiently far from the nozzle exit orifice (1.5mm) which serves as the reference point for nozzle axial distance. As seen in the bottom left inset, the standard deviation increases linearly with distance from the nozzle.

3. Calculation

The model is comprised of three parts that solve in seconds on a commercial desktop machine and can be controlled by a parametric search, multilayer tracking routine or an optimization algorithm. A block schematic of operations is presented in Figure 6. Physical constants and setup parameters are shown in Table 3. Each block is addressed in solving order.

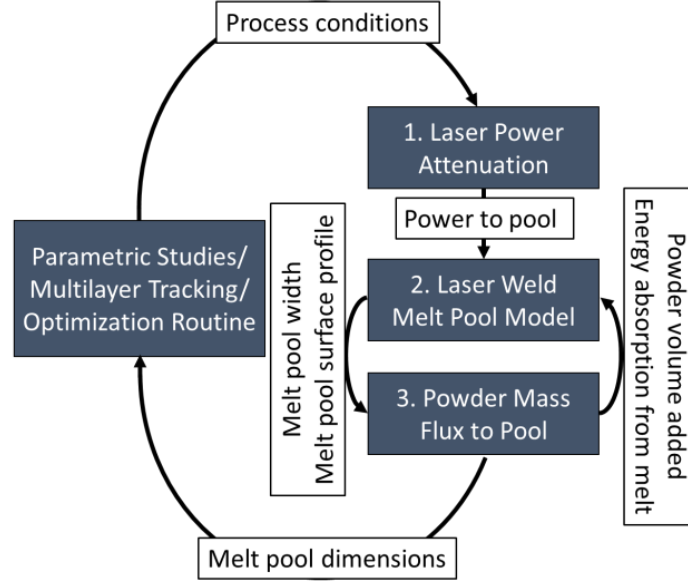


Figure 6. Overview block schematic of model solving routine. Blocks 2 and 3 require iteration before converging.

Table 3. Physical constants, experimental constants, and numerical parameters used.

Property	Symbol	Quant.	Units	Source
Density	ρ	$8.03 \cdot 10^6$	$\text{g} \cdot \text{m}^{-3}$	[40]
Thermal Diffusivity	α	$4.0 \cdot 10^{-6}$	$\text{m}^2 \cdot \text{s}^{-1}$	[41]
Heat Capacity [†]	C_p	0.5	$\text{J} \cdot \text{g}^{-1} \cdot \text{K}^{-1}$	[40]
Melting Temperature (avg T_{solidus} & T_{liquidus})	T_m	1425	$^{\circ}\text{C}$	[42]
Latent heat of fusion	L_f	270	$\text{J} \cdot \text{g}^{-1}$	[43]
Normal Spectral Emissivity (liq. iron @1064 nm)	ϵ	0.35	-	[44]
Experimental Constants				
Laser divergence half angle	θ_{laser}	2.3	deg	Measured
Laser focal working distance (+z is down)	WD_l^f	$-3.4 \cdot 10^{-3}$	M	Measured
Nozzle axis convergence working distance	WD_p^f	$1.07 \cdot 10^{-2}$	M	Measured
Argon carrier gas flow rate	v_{gas}	$6.3 \cdot 10^{-5}$	$\text{m}^3 \cdot \text{s}^{-1}$	Measured
Powder velocity [†]	v_{pow}	7.0	$\text{m} \cdot \text{s}^{-1}$	Measured
Powder divergence angle [†]	θ_{disp}	4.23	deg	Fit
Average Particle diameter [†]	D	$7.5 \cdot 10^{-5}$	m	Measured
Numerical Parameters				
N of elements, melt pool model		100	-	-
Convergence error criteria, power partitioning between powder, melt pool, and attenuation		<0.01	%	-

[†]Treated as constant at average value

In block 1, the nominal laser power delivered to the melt pool is attenuated by the powder cloud, which is treated as a continuous field not accounting for individual particles. The powder

cloud was characterized experimentally from the observation from previously described high speed video. For the conditions used, particle concentration was found to be Gaussian when sliced perpendicularly to the nozzle axis, and trajectories were largely unaltered by the argon flow after exiting from the nozzles. This can be analytically represented by treating mass flux for each nozzle as a 2D Gaussian distribution in the plane perpendicular to the nozzle axis, with a standard deviation that increases linearly along the axis of each nozzle, as shown in Figure 5.

Equations (1)-(3) show the coordinate transformation from the overall head assembly orientation (x,y,z; laser directed along +z axis) and single nozzle orientation (x',y',z'; center of powder flow is directed along +z' axis). Equation (4) governs the linear growth of powder dispersion with nozzle axial distance (z'). Equation (5) shows the powder flux as four superposed radially symmetric 2d gaussian distributions. Equation (6) converts this flux to a mass concentration distribution with the assumption of constant powder velocity.

$$x' = i(x + x_0) \cos \theta_{\text{axis}} - (z) \sin \theta_{\text{axis}} \quad (1)$$

$$y' = j \cdot y \quad (2)$$

$$z' = i(x + x_0) \sin \theta_{\text{axis}} + (z) \cos \theta_{\text{axis}} \quad (3)$$

$$\sigma = z' \tan(\theta_{\text{disp}}) + \sigma_0 \quad (4)$$

$$J(x, y, z) = \sum_{i=-1,1} \sum_{j=-1,1} \frac{F}{4} \cdot \frac{1}{2\pi\sigma^2} \exp\left(-\frac{x'^2 + y'^2}{2\sigma^2}\right) \quad (5)$$

$$C_m(x, y, z) = \frac{J}{v} \quad (6)$$

where i, j specifies the four powder feed nozzles, σ is the standard deviation of the powder flow field at a given axial distance from the nozzle, σ_0 is the fit standard deviation at WD=0, x_0 is the offset of the nozzle axis at WD=0, θ_{axis} is the angle of attack of the nozzle axis. All other parameters can be found in Table 2 and Table 3. Velocity and particle size are treated as constants

at the average values of 7 m/s and 75 μm in the current implementation, as this permits scalar transformation from mass flux to mass concentration to particle concentration.

Attenuation is found via the Lambert-Beer law [34] with the MATLAB[®] ODE45 solver:

$$\frac{dI}{dz} = -I \cdot A \cdot C_n(z) \quad (7)$$

$$C_n(z) = \frac{\iint C_m(x, y, z) dx dy}{V \cdot \rho} \quad (8)$$

where I is laser intensity (W/m^2), A is particle cross section area ($\text{m}^2/\text{particle}$), C_n is particle number density ($\text{particles}/\text{m}^3$), V is particle volume ($\text{m}^3/\text{particle}$), and ρ is the powder's material density (g/m^3). A constant emissivity of 0.35 for the molten pool energy absorption at 1064 nm was used [44]. Powder mass concentration is integrated over the beam cross sectional area, which varies along z with the beam radius $r(z)$ [45], which is fit to experimental data:

$$r(z) = r_0 \sqrt{1 + \left(\frac{z - z_f}{l_r}\right)^2} \quad (9)$$

where r_0 is the beam waist, z_f is the position of the focal plane, and l_r is the Rayleigh length.

Energy that is absorbed by the powder can either be delivered to the melt pool when the powder enters the pool, or it can be lost into the chamber if the powder particle fails to integrate into the part, as illustrated in Figure 7. From the schematic, it can be seen that for non-rebounding particles travelling through the laser there is a threshold z height, below which particles will integrate into the pool and above which particles will have a non-captured trajectory.

$$z_{threshold} = \frac{WD \cdot x_0}{b + x_0} \quad (10)$$

More rigorously, this threshold z height is the parabolic top intersection surface between the volumes of the laser profile and the irregular cone traced between the nozzle and melt pool; however, for narrow laser beams this can be treated as a single z value.

To demonstrate a typical calculation of energy delivery to the melt pool, an initial laser energy of 328 W is numerically attenuated to 314 W by the integrated concentration in the defined powder flow cloud as it travels from a working distance of 0mm to the top surface of the build at 10mm. The emissivity of 0.35 reflects most of the energy, leaving 110 W delivered into the material to calculate the melt pool dimensions in the next step. After melt dimensions have been calculated, the $z_{\text{threshold}}$ height can be calculated to account for energy absorbed by powder with trajectories that intersect the melt pool, in this case 9.5mm. The input power to the substrate is updated slightly to only attenuate from 0 to 9.5mm which delivers 317 W incident (111 W absorbed), and the calculation is iterated until error falls below the specified threshold of $1e-4$.

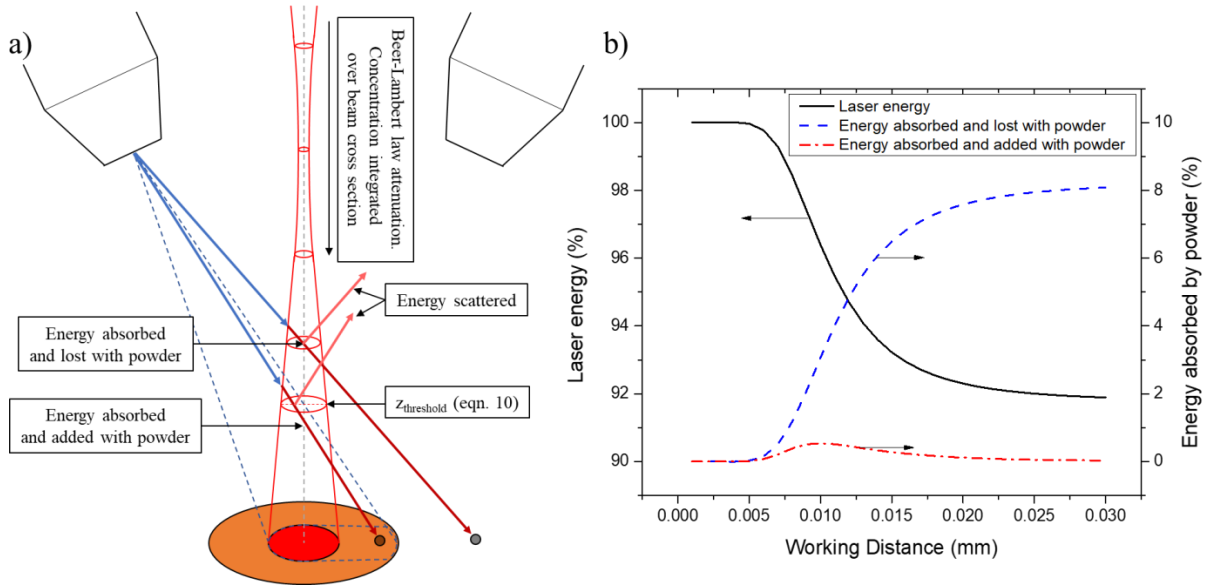


Figure 7. Energy partitioning as the laser is absorbed and scattered by powder in flight according to the Beer-Lambert law in Eqn. (7) and powder spray pattern in Eqn. (8).

In block 2, the dimensions of the melt pool are calculated using the isotherm migration method as implemented by Devesse [46], which reduces the thermal field evolved in a substrate

by a laser scanned across its surface to a finite element one-dimensional problem in mapped spherical coordinates that can be readily solved by the MATLAB® ODE23 solver. This is achieved through inverting the heat conduction equation to track the positions of fixed temperatures instead of changes in temperature at fixed positions. Latent heat of fusion is accounted for by imposing a Stefan condition on the melting isotherm ellipsoid; and as such differs from the Rosenthal solution.

The isotherm migration method provides a rapid, physically driven estimation of melt dimensions; however, it has several limitations. First, it assumes ellipsoidal isotherms to allow remapped spherical symmetry. So, following the previous example, for a delivered energy of 111 W, the melt pool is calculated to be a semi ellipsoid 0.54mm wide, 0.269mm deep, and 0.62mm long at a scanning speed of 16.9mm/s over 316l stainless steel. This calculation neglects the real power profile of the laser, convection within the melt pool, and convective and radiative heat transfer away from the top surface of the melt. These neglected physics can distort the shape of the melt pool away from this assumed shape [5], [47], and can be expected to become more inaccurate as the laser traverse speed increases and melt pools are lengthened. Additionally, no predictions are expected to be accurate in the keyholing regime where power density is high enough to vaporize metal, as the laser will interact with the vapor cloud, reflect multiple times, and back pressure will strongly displace liquid metal [8]. These inaccuracies therefore require that the melt pool model only be used under conditions that reasonably match these assumptions.

In block 3, the mass added to the melt pool is calculated by integrating the powder mass flux from Block 1 equation (5) across the area described by the perimeter of the melt pool:

$$\dot{m}_{melt} = \int_{y^-}^{y^+} \int_{x_0-a}^{x_0+a} J(x, y, WD) dx dy \quad (11)$$

$$y^+ = -y^- = b^2 \sqrt{1 - \frac{(x - x_0)^2}{a^2}} \quad (12)$$

where y^+ and y^- describe the boundaries of the melt pool perimeter ellipse with major and minor axes a and b and center $(x_0, 0)$ for a beam centered at $(0, 0)$ scanning in the positive x direction, in keeping with notation from Devesse [46]. The energy required to heat and melt this added powder from room temperature with no superheat is then calculated. So, following our previous example, the flow field from a 25 g/min powder feedrate is integrated over a melt pool with dimensions $a = 0.31$ mm and $b = 0.27$ mm to obtain 9.9 mg/s, which consumes 9.6 W of the available 111 W to bring the powder to a liquid state. The model then iterates between block 2 and block 3, subtracting the energy required to melt added powder from the energy available for establishing the melt pool boundaries, and recalculates the mass added. The model exits iteration when the difference between subsequent calculated added masses falls below 0.01% of the added mass.

With converged melt pool dimensions the following calculations can then be made [48]:

$$\frac{\dot{m}_{melt}}{S} = \bar{\lambda}_m = \bar{\lambda}_V \cdot \rho \quad (13)$$

$$\text{Average Deposited Layer Height} = \frac{\bar{\lambda}_V}{H} \quad (14)$$

$$\text{Mass Capture Efficiency} = \frac{\dot{m}_{melt}}{F} \quad (15)$$

where \dot{m}_{melt} is the mass flow rate into the melt pool (g/s), S is the traverse speed (m/s), λ_m is the linear density of mass added (g/m), $\bar{\lambda}_V$ is the linear density of volume added (m^3/m), or in a cross section, the area above the substrate level, ρ is the density at room temperature (g/m^3), H is the spacing of adjacent raster lines (m), and F is the powder flow rate (g/s). The average deposited layer height (m) is calculated purely from the volume deposited and does not account for top surface height variation from track to track.

4. Results

The characteristic measured key dimensions of the cross sections of the 258 single track experiments were measured. A representative cross section describing these measurements is shown in Figure 8. While statistical [33], and empirical [34] correlations can readily be developed for this data, such relations tend to be non-extensible between AM systems, and is not the focus of the present work, which uses these dimensions for model validation.

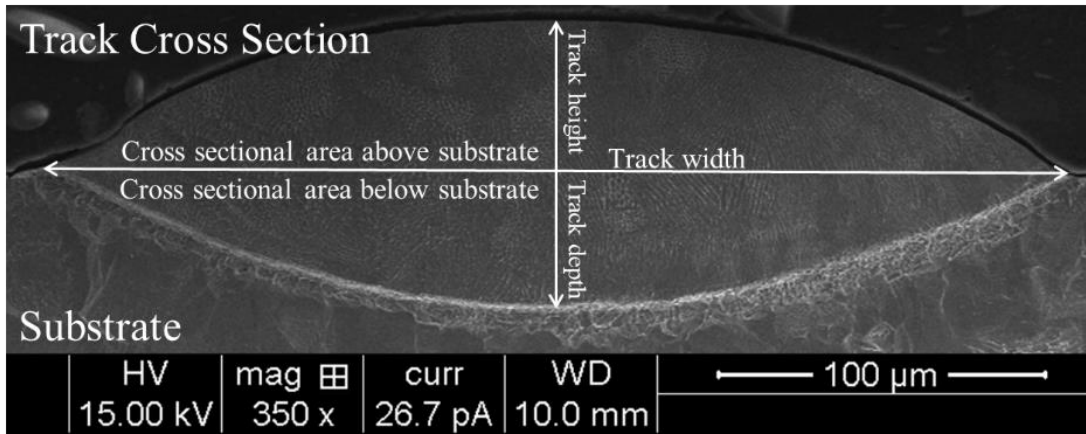


Figure 8. SEM micrograph of an etched 316L single track. Measurements were taken of the width, height, depth, and cross section area above and below the substrate for 258 tracks deposited at unique conditions.

To use this data for validation, the model was executed for each matching combination of power, speed, and powder feed rate used to generate the single tracks, and are compared in Figure 9. Melt pool height predictions scatter strongly, but overall are fairly centered on the measured values. Melt pool widths were under predicted and melt pool depths were over predicted, which can be a consequence of the assumptions made by the cylindrical symmetry of the migrating isotherm melt pool model. Melt pool cross sectional areas were better predicted than other dimensions, which can possibly be due to reduced measurement sensitivity to partially molten particles welded to the track surface (a large source of variation for the thinner tracks).

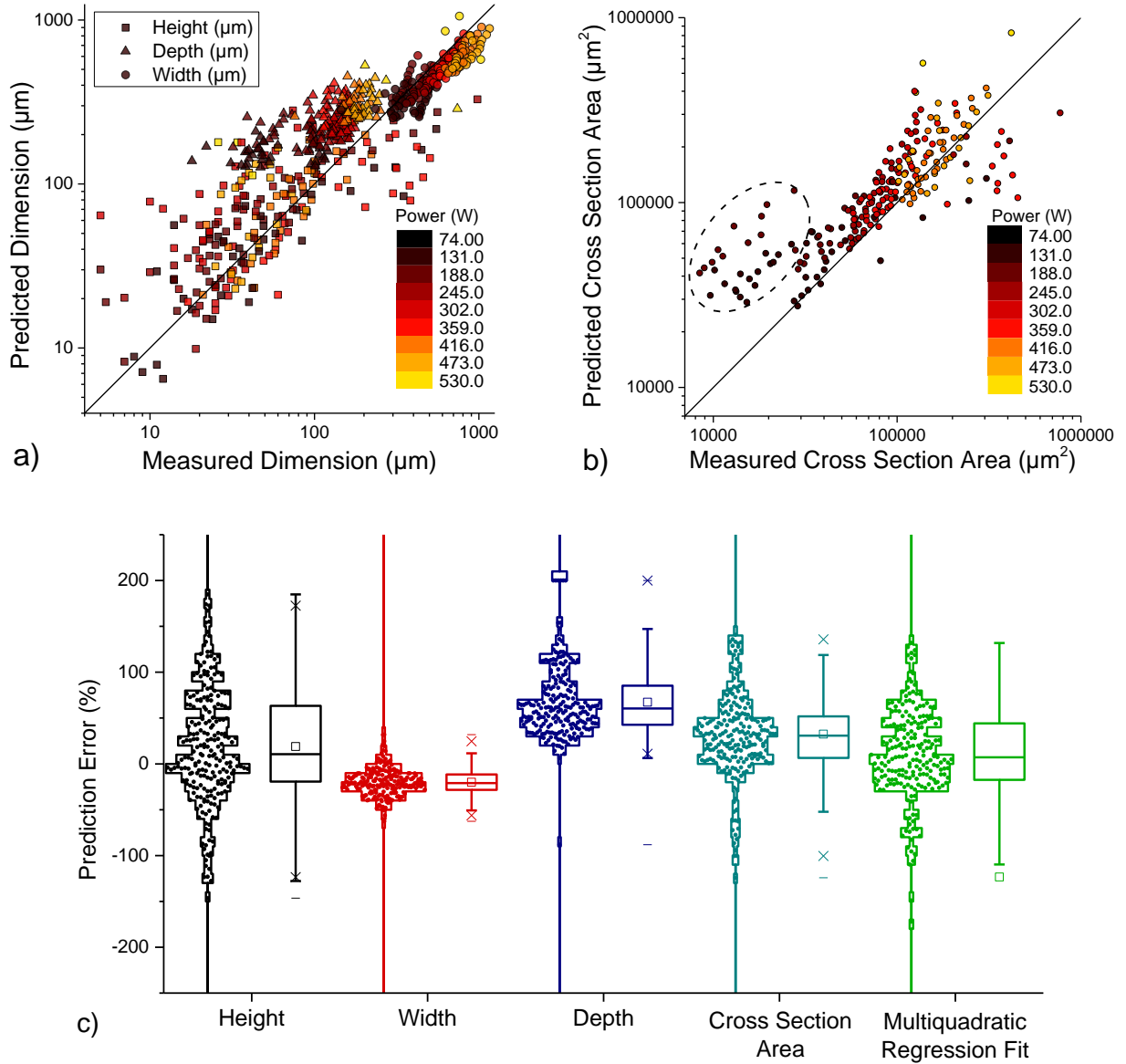


Figure 9. In a) and b), predicted and measured single track dimensions are compared. Panel c) presents the distribution of prediction error for all tracks. The model overpredicts melt pool depth and underpredicts width, which is partially a consequence of the spherically symmetric coordinates and point heat source required by the thermal model. The model better predicts overall track cross sectional area, which correlates with volume of molten material. Cross sectional area predictions compare favorably against a raw statistical multivariate (P,F,S) quadratic regression fit of cross sectional area, indicating that much of the prediction error is contributed from variability in the measured dataset.

A series of low power tracks whose melt volumes are strongly over predicted are highlighted by black dotted circles in Figure 9. These do not follow trends established at higher

powers, and demonstrate the breakdown of the model as the melt pool widths approach the diameter of the laser spot size and the violation of the point heat source assumption.

While large systemic error was seen in individual dimensions due to the thermal model's simplifications, the total amount of molten material depends on the energy balance between incoming radiation and dissipated heat, which is captured with more accuracy by the model and is shown to capture much of the variability in the measurements. Although prediction accuracy for individual measurements is not highly reliable, the model is built from physical arguments, material constants, and measured system properties only, and only uses empirical fitting coefficients to describe physically quantifiable model inputs, without fitting to model predictions. As such, it is extensible to other parameter sets and machine setups, as long as the discussed assumptions of the model are not severely violated, i.e. laser incident intensity low enough to avoid keyhole mode, conduction is the dominant heat transport mechanism, ect. Different material systems will can have different processing windows where the assumptions made remain valid, and the model does not preclude the many different deposition mechanisms that may dominate over the presented conditions, so it remains a first order estimate that should be experimentally confirmed. Given the model's ability to capture a significant fraction of the variation in a noisy dataset, it is considered functionally valid for the purpose of investigating trends in overall process stability, with the caveat that discovered trends be confirmed with additional experimentation, as discussed below.

5. Discussion

5.1 Passive working distance stability via powder distribution

One issue in open loop DED systems is that there is no explicit method to maintain the same working distance throughout the course of deposition. Parameters must be selected to deposit

the correct amount of material to match the target layer thickness; any inaccuracy could be expected to propagate throughout deposition, yielding highly overbuilt or underbuilt geometries. However, this does not consider that the amount of material deposited can vary over time with changing working distance. To quantify this variable behavior, the model was executed at a range of different working distances, and plotted against the average deposited layer height, as seen in Figure 10. Figure 10a illustrates the shape of the calculated mass concentration in the powder cloud. Figure 10b shows how the mass capture efficiency dramatically changes with working distance (plotted in reverse to match the schematic) as the melt pool is moved to into and out of the ‘focal point’ of the powder flow. This creates a deposited layer whose thickness can be found by dividing the upper cross-sectional area by the machine set hatch spacing, which is here 0.37 mm for 33% width overlap.

Figure 10b also contains experimental data from measuring cross sections of single tracks taken at different working distances (while maintaining laser focal position relative to the substrate). It can be seen that even in the absence of any empirical fitting, using only measurable physical quantities, the model reproduces experimental tracks satisfactorily.

Table 4. Definitions for terms and symbols.

Nomenclature:			
WD	Working distance	h_{set}	Set height increment for nozzles
WD _s	Passively stable working distance	h_{dep}	Average deposited layer height
WD _U	Threshold for WD instability	f_l	Laser focal length (constant)
z_f	Laser focal plane	l_{def}	Laser defocus length

Over the course of depositing many layers, the working distance will change if the amount the nozzles are moved upward is larger or smaller than the actual average deposited layer thickness. This change in working distance per layer is calculated according to:

$$\Delta WD = h_{\text{dep}} - h_{\text{set}} \quad (16)$$

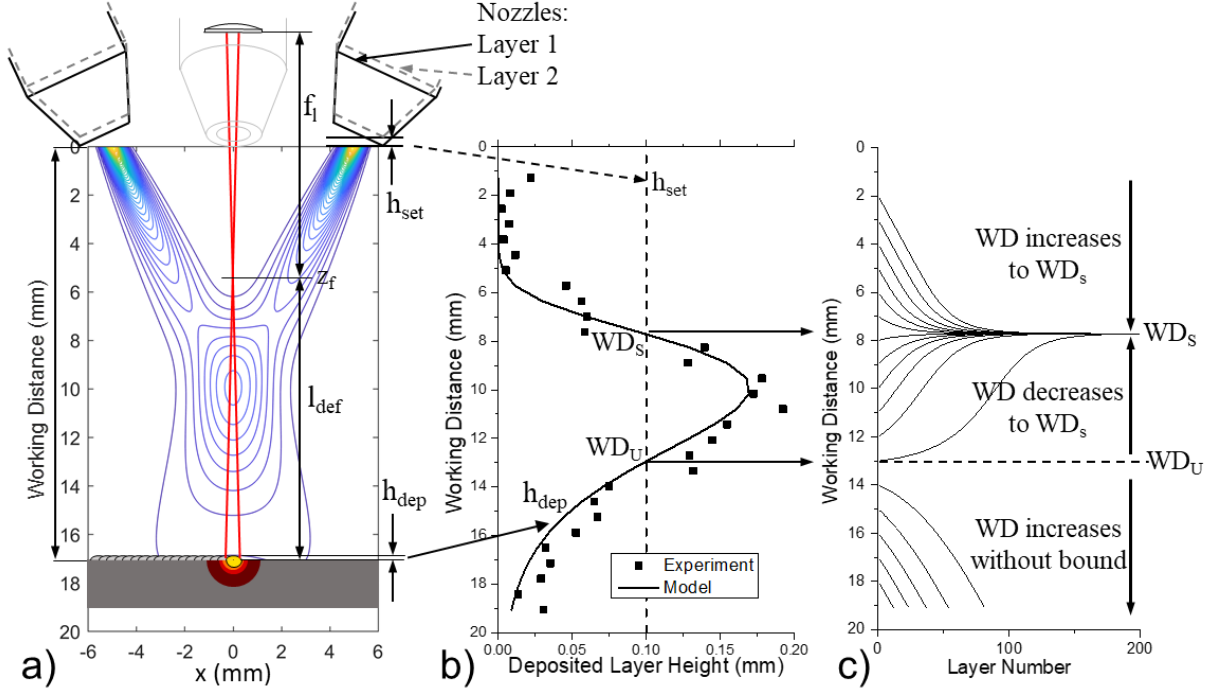


Figure 10. Mechanistic demonstration of how powder spray pattern alters working distance to a passively stable value. In a), powder spray concentration predicted by the model is shown in blue contours. h_{set} is the increment the nozzles are programmed to move between layers, and h_{dep} is the actual deposited layer height calculated with equation (11). In b), h_{set} (vertical dashed line) and h_{dep} (curve) are compared to each other. The difference between h_{dep} and h_{set} creates layer-to-layer change in the working distance as per equation (16). In c), it can be seen that over many layers, any $WD < WD_U$ converges to a single stable value at WD_s , and any $WD > WD_U$ is unstable. In b), h_{dep} is validated with experimentally measured data from single tracks.

The shape of this curve implies that working distance will either converge to a passively stable working distance at crossover point WD_s , or will increase without bound for all working distances greater than point WD_U . This is shown in Figure 10c, which tracks how the working distance evolves over many layers, given unchanging deposition parameters. The position of stability points WD_s and WD_U in Figure 10b will shift with changes to the set layer height. This passive stability point has been the core mechanic used, knowingly or unknowingly, by every study performed on open-loop L-DED systems for obtaining geometrically accurate deposition. It sets up a working distance feedback loop that opposes process perturbations.

The practical importance of this phenomena has been qualitatively recognized before [28]–[30], but is now quantified in two ways. First, the slope of the curve at point WD_S in Figure 10b can be seen as the corrective influence that enforces the stable working distance. A steeper crossover will require less distance in the Z build direction to converge back to the stable working distance after a perturbation. This will here be termed working distance correction response:

$$\text{WD Correction Response} = \frac{d(h_{\text{dep}})}{d(WD)}, WD = WD_S \quad (17)$$

Third, the difference in working distance between the stability point A and instability point B can be seen as a measure of the maximum working distance deviation that the system can compensate for. This metric collapses to zero when the machine set layer height exceeds the maximum possible deposited layer height. This will here be termed height deficiency tolerance:

$$\text{Height Deficiency Tolerance} = WD_S - WD_U \quad (18)$$

5.2 Thermal buildup effects on passively stable working distance

Frequently in L-DED, part geometry is such that thermal dissipation from the part does not balance with the incoming heat from the laser, resulting in a buildup of heat throughout the course of the build. This can impact working distance stability, as shown in Figure 11a. A higher base temperature reduces the amount of heat that is required to elevate temperature to the melting point, increasing melt pool widths and increasing powder capture efficiency overall. This alters the passively stable working distance as shown in Figure 11b. It can be anticipated, therefore, that for geometries such as thin walls that have low layer times and less time to dissipate heat, the working distance will tend to shrink and melt pool size will grow, a result that has been numerically predicted by other work [25].

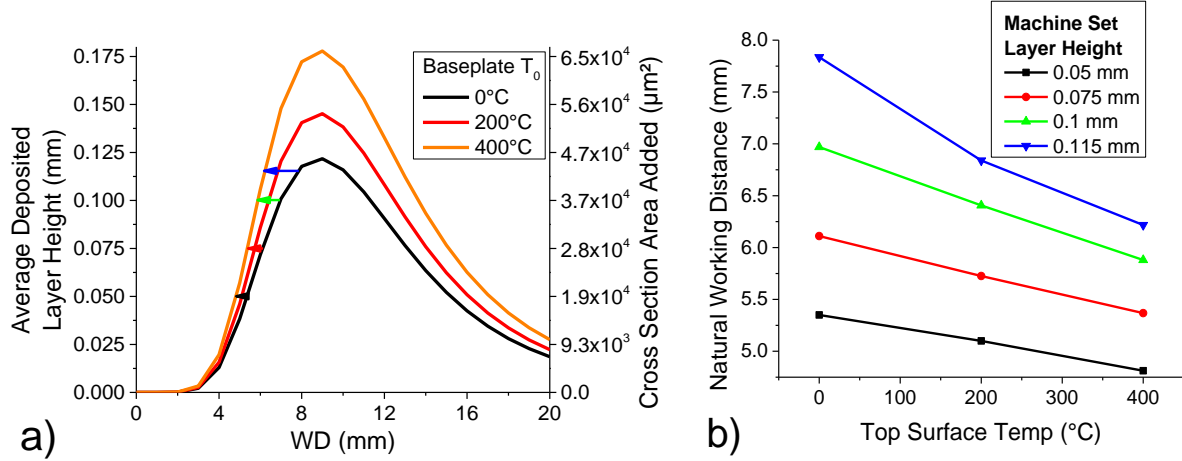


Figure 11. Effect of thermal buildup on a) track dimensions and b) stable working distance at several set layer heights. Arrows indicate resultant shift of passively stable working distance for four different set layer heights.

5.3 Flow distribution effects on passively stable working distance

To further study process effects on the stable working distance, two parametric studies are presented in Figure 12, where nozzle axis angle and powder flow dispersion angle are varied.

Powder dispersion is a function of several parameters, namely nozzle design, carrier gas velocity, particle size, density and shape [22]. The change in the powder flow cloud shape from tightening the dispersion angle can be seen in blue in Figure 12. Decreasing the powder flow dispersion increases the overall mass capture efficiency, which increases the maximum possible deposited layer height. Additionally, decreasing powder dispersion increases the working distance correction response $d(h_{\text{dep}})/d(\text{WD})$ at the stable working distance, meaning that any deviations from the stable working distance will be more strongly corrected.

Nozzle axis angle is set by machine design. The change in flow shape can be seen in red in Figure 12; increasing the angle between the nozzle axes and the central laser axis has a deleterious effect on the stability metrics. This can be attributed to two causes. First, the melt pool is less perpendicular to the flight path of the particles, which reduces mass flux through the perimeter of

the melt boundary. Second, distance between the nozzles and the convergence point is increased with higher angles, which permits higher powder flow dispersion at the melt pool.

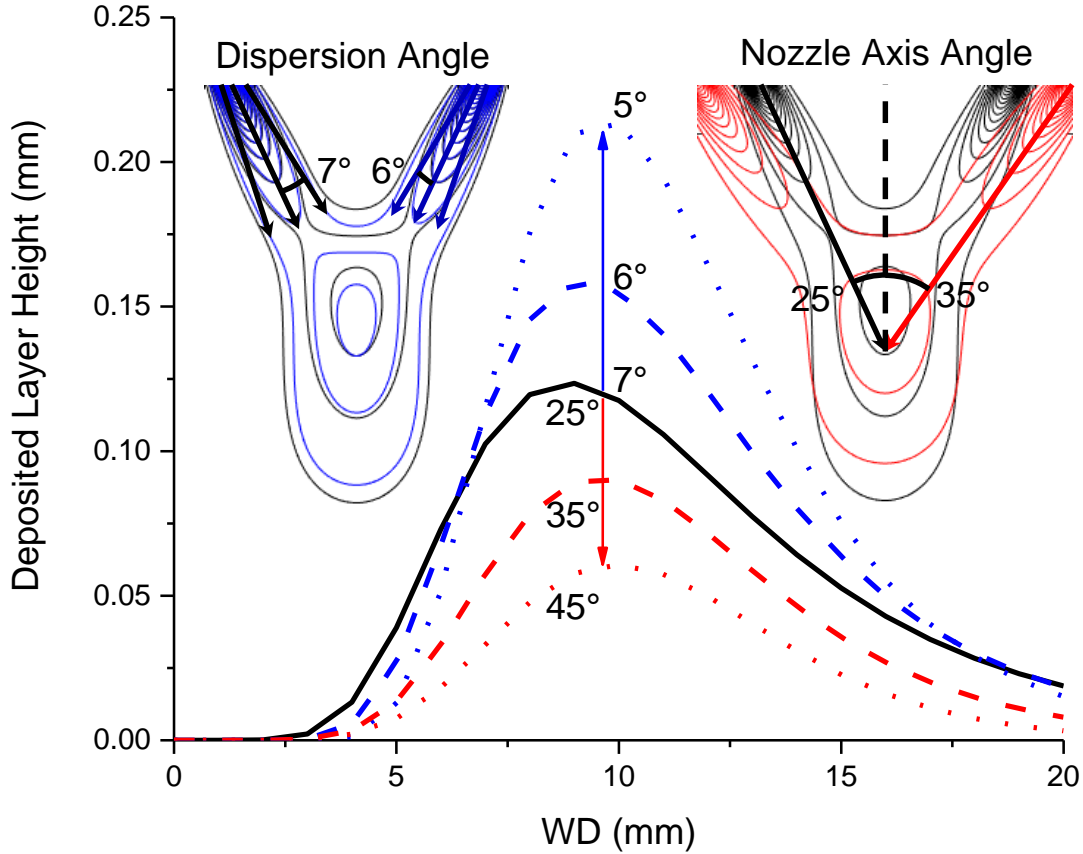


Figure 12. Effect of varying powder flow dispersion angle and nozzle axis angle on working distance stability.

6. Conclusions

A passive, self-regulating stability feedback loop present in L-DED was studied by constructing and validating a MATLAB model. The model consists of three components that represent a) the concentration distribution of the powder spray pattern, b) the attenuation of laser power through the spray, and c) the heat transfer, shape, and mass transfer into the melt pool. The model does not require any empirical or fitting coefficients and is based on physically measurable quantities only, which permits it to be used for other material systems and DED machines within the bounds of validity of the assumptions discussed. Experimental validation was performed with

a set of 258 single track experiments at variable powers, powder feed rates, speed, and working distances. While the spherical symmetry condition of the thermal model introduces systemic biases in melt pool dimension predictions of width and depth, the model predicts total melt volume and captures much of the variability of the experimental dataset, and compares favorably against statistical fitting. The main results are summarized as follows:

- The powder spray pattern from four nozzles causes powder capture efficiency to vary as working distance changes. When working distance is not explicitly controlled, it will either converge to a single stable level characteristic of a set of process conditions, or increase without bound.
- Passive stability can be described with two metrics defined in the present study: working distance correction response and height deficiency tolerance.
- As surface temperature of underlying material increases, mass capture efficiency will increase and shift the passively stable working distance closer to the nozzles.
- Powder flow dispersion angle is a function of powder size, shape, carrier gas flow and nozzle design and has a strong impact on passive stability through sharpening or softening the powder focal boundaries and modifying peak mass capture efficiency.
- Increasing the nozzle axis angle defocuses the powder flow and reduces mass capture efficiency and working distance stability.

CHAPTER TWO: OBSERVATIONS OF PARTICLE-MELT POOL IMPACT EVENTS IN DIRECTED ENERGY DEPOSITION

Published in *Additive Manufacturing*, Aug 1, 2018

Abstract

In the rapidly growing field of Additive Manufacturing (AM), the Laser Directed Energy Deposition (L-DED) process is the focus of intense technical attention due to its potential to generate high quality components with location specific composition and microstructural control. Despite the variety of experimental and modelling efforts devoted to the subject, no studies directly observe the interactions between individual powder particles and the liquid pool of metal at a high enough temporal frequency to characterize these discrete contact events. The frequency and nature of these powder-pool impingements govern overall process behavior, and are a poorly quantified fundamental building block of L-DED. In this work, we report novel results in which the melt pool is imaged at up to 200,000 frames per second, with pixel resolution of up to 3.6 μm . Video images reveal that particles often impact and float on the surface of the melt pool for several hundreds of microseconds before melting into it. Further incoming particles were observed to rebound from the melt pool by these floating particles. Through modelling this process analytically, particle self-shielding is shown to impose unavoidable upper limits on overall powder capture efficiency for the L-DED process.

1. Introduction

As illustrated in Figure 13, Additive Manufacturing (AM) by Laser Directed Energy Deposition (L-DED) is a process where a high power laser (a) is focused on a substrate, melting a small pool of material (b) into which powder feedstock is injected via spray nozzles (c). The laser and powder feeders are rastered relative to the substrate in the X-Y plane (d) in a shape

corresponding to a single cross section of a desired part. When a full layer is complete, the assembly moves upward in the Z axis and the entire process repeats until a part is deposited. The process has established a reputation for net shape forming parts with mechanical properties approaching or exceeding those in wrought or annealed conditions for different alloy systems [49], but it can suffer from lack of repeatability and predictability due to sensitivity to many competing process influences.

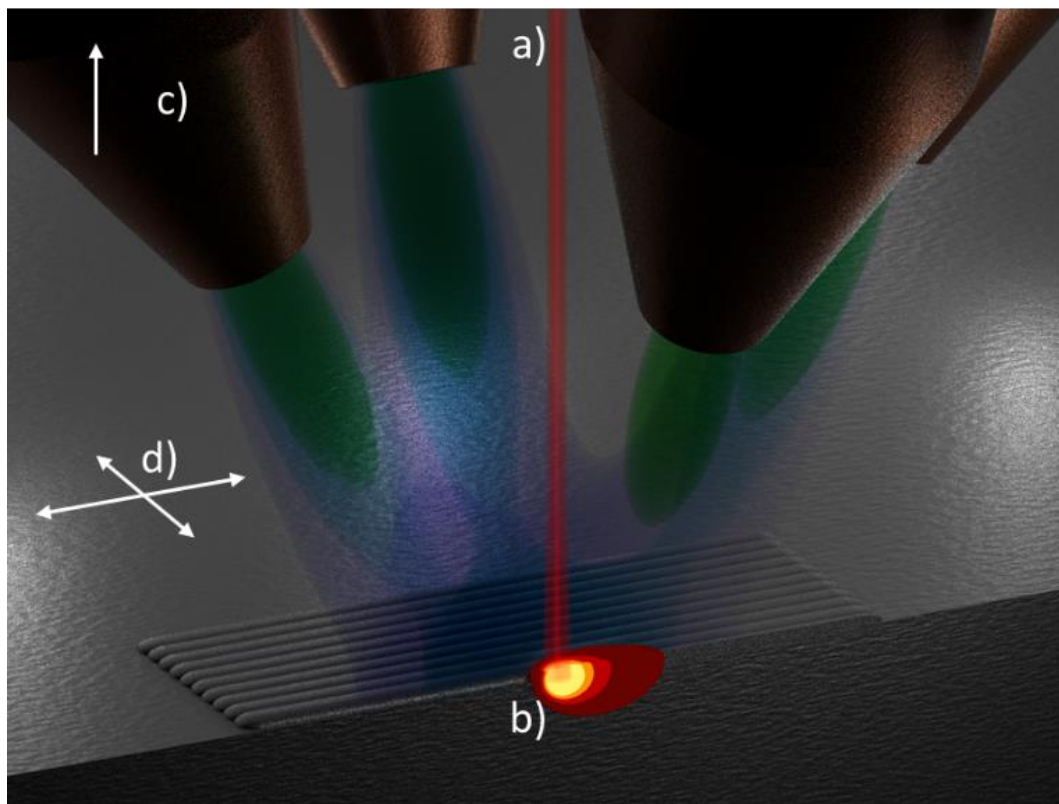


Figure 13. Schematic of L-DED process; a laser (a) forms a molten pool of metal (b), into which powder is fed from spray nozzles (c). The substrate is rastered in the X and Y directions (d) to form a single layer of material, after which the nozzle assembly is moved upward and the process repeated.

A large contributor to the difficulty in predicting the behavior of the L-DED process is the highly stochastic interaction between particles with variable sizes, velocities, shapes and trajectories [22] with a pool of molten metal that is constantly being reshaped by particle impact events, surface tension, internal fluid [50] and external gas convection, and back pressure from

vaporizing metal [9]. Observing the relative influence of these effects and recombining the obtained knowledge into holistic process models is an ongoing struggle, as many of these influences are experimentally inseparable.

In order to parse the many physical aspects of the L-DED and other laser based additive manufacturing systems, numerous studies have employed optical in-situ characterization techniques. These measurements tend to focus on two key areas: the trajectories and mass capture probabilities of feedstock particles after they exit the nozzle [22], [51], [52], and the size, shape [21] and temperature distribution of the melt pool [12], [15], [53], [54]. Particle fields can be observed with long exposure images, that give a statistical sense of concentration distribution [55], or alternatively with very short exposures or short light pulse images that reduce motion blur and resolve individual particles as points or streaks for counting, shape analysis, and velocity measurements [51]. Melt pool images can be captured from a top-down view coaxial with the primary heating laser [54] or from the side for height profile information [11]. Wavelength filter selection determines the physical process providing image contrast; one can potentially cut out blackbody thermal radiance and use additional illumination for morphology, or limit thermal radiance to selected wavelengths, which is useful for pyrometric measurements [12].

While highly informative, these studies focus on quantifying powder motion and thermal histories at time and length scales too large to detail the momentary interaction between individual powder particles as they are accepted into the melt pool. This can be partly attributed to technological limitations of high speed video and optical technology; as exposure times are decreased and magnifications are increased less radiance is available per pixel to generate signal. Furthermore, frame rate trades off with image resolution as cameras are limited by either data transfer rates, in the case of camera systems C1, C2, and C4 in Table 5, or total video length, for

camera C3, which uses a different memory format. To provide context for the technical challenge, a typical average particle velocity for L-DED is on the order of 5-10 m/s [22], which means that if a $\sim 100\text{ }\mu\text{m}$ particle penetrates into the melt pool without slowing down, the interaction would occur in roughly 10-20 μs . In other words, at a frame rate of 100,000 frames per second, a particle would be reasonably expected to only be visibly interacting with the pool surface for one or two frames, and could suffer from motion blur.

One notable study by Matthews et al [14], which did employ high magnification, high speed video, recorded particles at 500 kHz being violently drawn in and ejected by the vaporizing melt pool in a powder bed Selected Laser Melting (SLM) system. While melt pool sizes are smaller and traverse more quickly than in a L-DED system, valuable insight about the formation mechanism for powder ‘denuded’ zones was obtained. No corollary work at these spatial and temporal resolutions has been published for a powder feed system.

With these technical limitations of FE modelling and optical imaging in mind, an unaddressed gap in the AM literature becomes apparent: what precisely happens when a sprayed particle contacts the surface of the melt pool in a powder fed L-DED system? How can the speed and momentum of particles in flight influence interactions with the melt pool? How do such interactions influence the character of the overall process? In this work, strategies are developed to overcome the technical challenges to imaging such melt-particle interactions to provide an experimental foundation to answer these questions. Video is presented demonstrating a wide range of behaviors, including particle retention on the melt pool by surface tension. Finally, mathematical relationships are derived from physical arguments to estimate the implications on overall system performance.

2. Experimental Methods

The Optomec 750 Laser Engineered Net Shaping (LENS)[®] system used for this study has four powder feed nozzles with ID 1.12 mm angled 25° off the Z axis. The system is outfitted with a IPG Photonics YLR continuous multimode fiber laser at 1064nm with a tophat power profile. The laser was used in the ‘underfocused’ condition with the focal plane set to 6.7 mm below the substrate, for an approximate spot diameter of 0.94 mm. The powder focal plane was set to 1.9 mm below the substrate with a working distance of 8.76 mm. All depositions for the study used a measured power output of 325 W with a scan rate of 16.9 mm/s, a nominal powder mass flow rate of 30 g/min and measured argon flow rate of 3.78 L/min. Feedstock powder was gas atomized 316L stainless steel provided by Carpenter, Inc. in the nominal diameter size range of 45-105 μm . The substrate material was rolled 316L stainless 4.76 mm thick.

Four high-speed cameras ($\geq 10,000$ fps), four lens systems, and three illumination systems, listed in Table 5, from three vendors were used to image the powder flow field and melt pool of an Optomec 750 LENS[®] system. Vendors were Elite Motion Systems (C1), Vision Research (C2), and Hadland Imaging (C3, C4). Video setup configurations presented in Table 6 correspond to codes provided in Table 5.

Table 5. Codes for equipment used in video setups.

Camera		
Code	Make	Model
C1	Photron	SA-Z
C2	Phantom	V2512
C3	Shimadzu	HPV-2
C4	iX	i-SPEED 720
Lens System		
KC	Infinity	KC VideoMax
K2	Infinity	K2 Distamax
NV	Navitar	Zoom 6000
NK	Nikon	Micro-Nikkor 200 mm
Lighting System		
640	Cavitar	Cavilux Smart (640 nm)
808	Oxford	Firefly (808 nm)
LED	Edmund Optics	SugarCUBE Ultra White
XL	No lighting	
Filter		
BP6	Bandpass filter (640 nm)	
BP8	Bandpass filter (808 nm)	
SP	Shortpass safety window, OD>3 @ 805-870 nm, OD>5 871-1070 nm	
XF	No filter	
Atmosphere		
AR	Argon in sealed glovebox, <20 ppm O ₂	
FL	Argon, flowing through powder feed nozzles at 3.78 L/min	
ATM	Ambient atmosphere	

Table 6. Sample captured videos and setup parameters

Powder Flow Videos				
Fig.	Setup code	FOV (mm)	Framerate (kHz)	Observed:
2a.	C2-NK-LED-XF-ATM	27.9x22.1	140	Influence of substrate on particle trajectories
2b.	C4-K2-640-XF-ATM	5.7x4.2	30	Individual particles with satellites resolved, velocities single nozzle measured
2c.	C4-K2-640-XF-ATM	15.3x11.1	10	Particle concentration density, dataset for probability estimates
2e.	C1-KC-LED-SP-ATM	12.4x5.4	100	Effect of laser & melt pool on trajectories
4c.	C2-NK-XL-SP-ATM	11x22	200	Thermal field trailing melt pool, rebound particle vaporization
Melt Pool Videos				
3a.	C1-KC-LED-SP-ATM	4.4x1.8	200	Silhouette of particles impacting melt
3b.	C3-NV-XL-XF-FL	1.1x0.93	63	Individual particle-melt impact events
4a.	C3-NV-XL-XF-FL	1.1x0.93	63	Particles float and drift on melt pool surface or freeze to the bottom of the melt pool
5a.	C3-NV-XL-XF-FL	1.1x0.93	63	Floating particle rejecting incoming particle

Four filter configurations and a variety of magnifications were used to optimize video quality. Specific configurations presented in Table 6 were driven by the information desired. The two illumination lasers were used in conjunction with their respective bandpass filters to produce topological information, producing satisfactory images of the trajectories of particles in flight. Another configuration used shortpass safety glass without the bandpass filters to permit collection of blackbody irradiance from the heated melt pool and particles. This permitted a qualitative sense of the distribution of heat through the melt and part, particularly for camera C2, a color model.

In order to characterize the interaction between individual powder particles and the melt pool, both lower magnification, lower speed videos were recorded to trace powder particle trajectories as well as higher magnification, higher speed videos to capture the discrete contact events and associated flow of the melt pool. The optimal configurations identified in this study that facilitated this information are listed in Table 6.

While the above configurations were satisfactory in reproducing lower magnification Particle Image Velocimetry (PIV) measurements reminiscent of characterization of powder flow trajectories in laser cladding [16], visualizing the interaction of individual particles with the melt pool required further optimization. Higher magnifications of up to 16x and higher frame rates up to 200 kHz limited the ability of secondary lasers to sufficiently illuminate the object with camera C3, so wavelength filters were removed in videos in Figure 15, Figure 16, and Figure 17 as detailed in Table 6, allowing the primary fiber laser light to provide sufficiently intense illumination. Additionally, this permitted tighter apertures to increase depth of field. Lowering powder feed rates allowed for a less obstructed view of the melt pool and successfully permitted observation of individual particles entering the melt pool.

After deposition, samples were sectioned via Electronic Discharge Machining, polished and etched with nitric and hydrochloric acid. Cross sections were imaged with optical microscopy.

3. Results

In Figure 14, concentration, and velocity measurements are collated to characterize the spray pattern in the used L-DED system. Full video is available in the online supplementary material. Particles were recorded rebounding off of a substrate (a), in flight from a single nozzle (b), particles in free flight (c), and the associated spatial concentration distribution was calculated from over one million individual identified particles (d). Particles were visualized during deposition of a single track of material (e), and in (f) trajectories were traced with open particle tracing software MOSAIC [56]. A scatterplot of identified velocities is presented in (g).

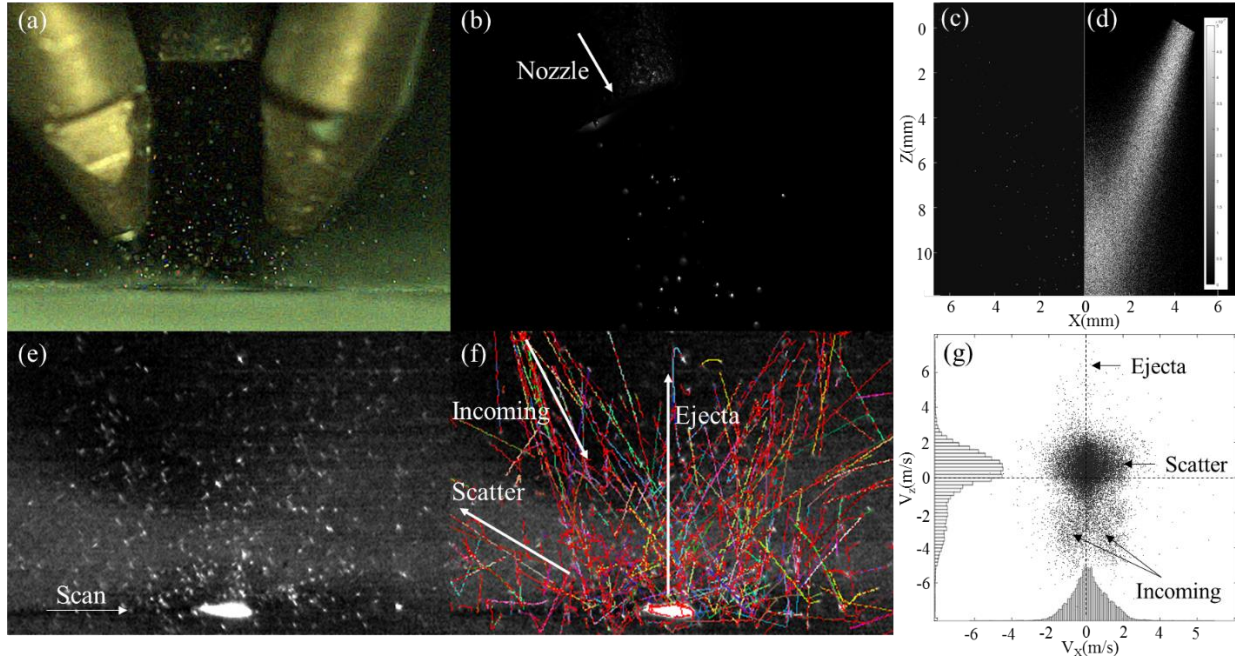


Figure 14. Characterization of powder spray pattern with high speed video. Video is available in the supplementary material. In (a) straight particle trajectories are diffusely reflected by a substrate. In (b) a single nozzle spray is observed, in (c) lower speed video (10 kHz) provides a 1 million particle dataset to identify spatial concentration of the spray (d). In (e) a single track of material is deposited, which with trajectory tracing software MOSAIC (f) reveals three particle flight modes – incoming particles sprayed from the nozzle, diffuse scattered particles, and particles ejected rapidly upward by metal vaporizing from the melt pool surface. Velocity components are plotted in (g).

In Figure 15, the melt pool during deposition of a single track of material was imaged under two different illumination conditions with the intent of tracing individual powder particles as they interact with the surface of the melt pool. In Figure 15a, particles are silhouetted by the thermal radiance of the melt pool. Figure 15b shows still images where illumination is provided by removing the shortpass wavelength filter, allowing the intense, 325 W from the primary fiber laser light at 1064 nm to scatter off the reflective surfaces of the particles and melt pool. This compensates for poor illumination from high magnification and short exposure times. This technique is also used in generating Figure 16a and Figure 17a.

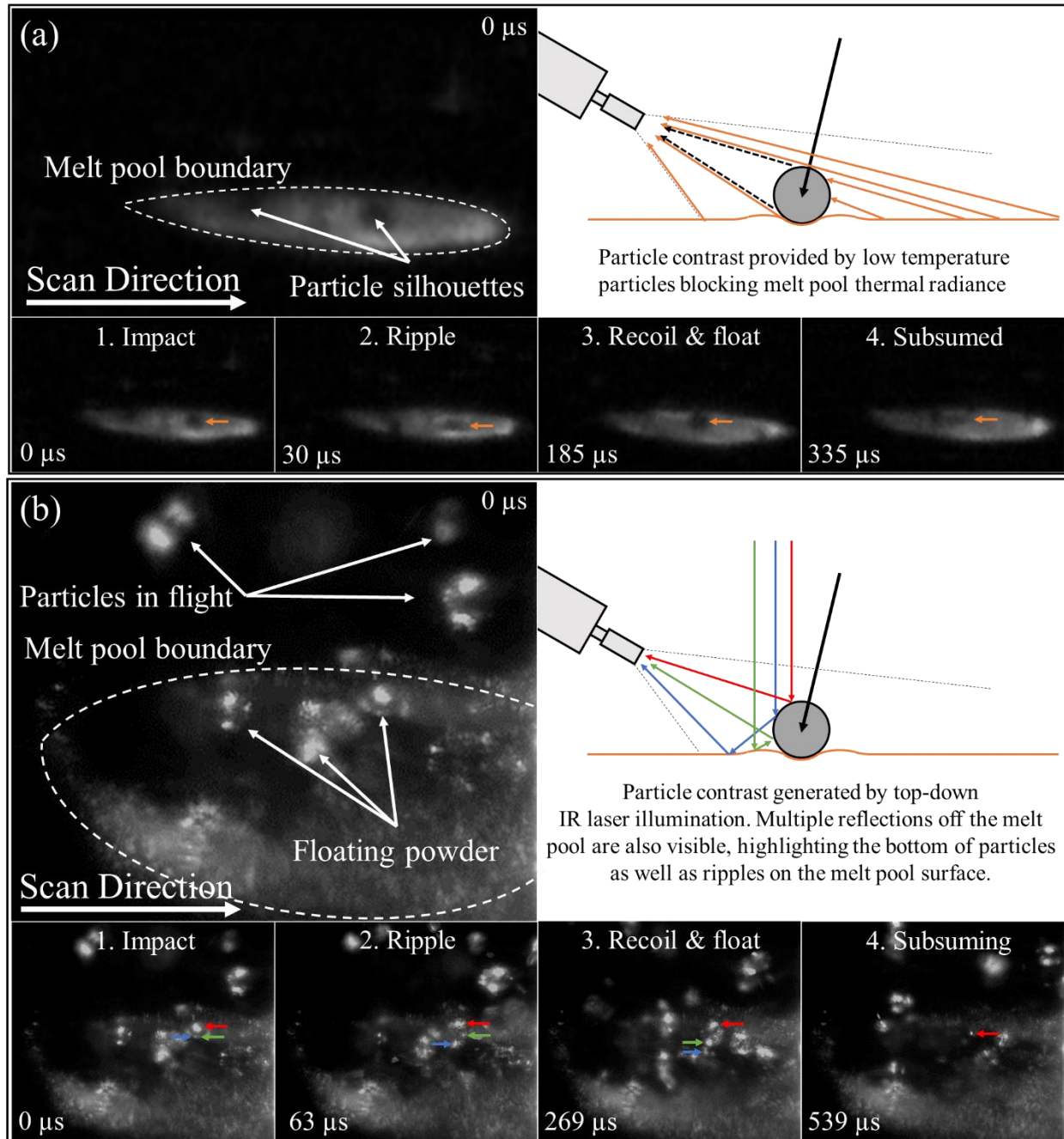


Figure 15. High speed videos demonstrating powder – melt pool interactions. Video is available in the supplementary material. Two illumination conditions were used, particles seen in silhouette from thermal radiance collected from the melt pool (a) as well as from unfiltered reflected illumination from the primary laser (b). Particles do not penetrate the surface, but instead impact (1.), displace molten material forming a ripple (2.) float for a brief residence period (3.) before subsuming (4.). Color coded arrows highlight generated contrast points tracking the particle through these characteristic stages.

Two micrographs of etched cross sections of particles frozen on the melt pool surface are presented in Figure 16b and Figure 16d. These represent the two morphologies commonly observed, where original gas atomized dendrites were still present in the particle as well as particles that have a cellular, directional solidification pattern more commonly found in L-DED parts.

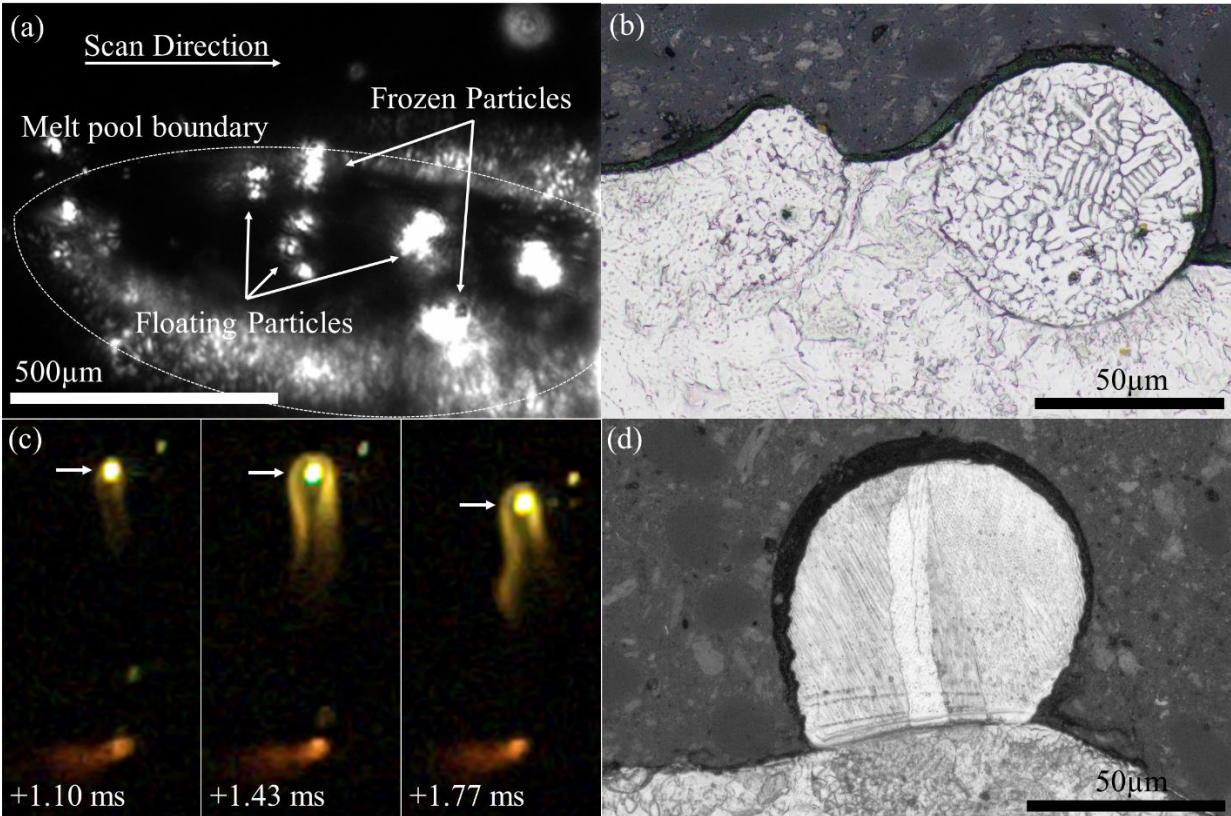


Figure 16. Two distinct formation origins for particles attached to external surfaces. Video is available in the supplementary material. In (a), particles can float on the surface of the melt pool, or freeze to the bottom when nearer the melt pool periphery; this can result in particles never fully melting as the melt pool solidifies around them, as shown in (b). In (c), a slow-moving particle passes through the path of the heating laser, melting and partially vaporizing it. These particles can land and solidify on available surfaces, as seen in (d).

4. Discussion

4.1 Characterizing Incoming Powder Trajectories

To characterize the spatial and velocity distribution of the powder flow cloud of the L-DED system, video under several conditions was recorded, as seen in Figure 14. In (a), motion of individual particles is clearly resolved, revealing that for the chosen particle size and gas flow

parameters, trajectories are straight after leaving the spray nozzles, and particles are diffusely reflected off of the rough substrate surface. In (b), a higher magnification image of a single nozzle reveals that few particle-particle interactions occur at the nozzle exit, as well as a high concentration of particles with satellites spinning at rates faster than is resolvable at the chosen frame rate. In Figure 14c, which recorded a larger field of view of the whole spray pattern, images were recorded at a lower frame rate (10,000 frames per second) to permit a larger statistical dataset of over one million particles to be identified to find the particle concentration of the powder cloud.

In Figure 14, the velocities of the powder cloud were further quantified during deposition of a single track of material in (e) by tracking particle trajectories using the open software MOSAIC [56]. Trajectories are highlighted in color in (f). Upon plotting the components of the velocities identified, three natural groupings of particles can be observed – incoming particles on their initial approach immediately after being sprayed, moving at 2-5 m/s; scattered and rebounding particles moving slower in every direction; and a small set of particles rapidly moving upward at up to 6-8 m/s as they are caught and ejected by the plume of metal vaporizing off the surface of the melt pool. These traced concentration distributions and trajectories provide baseline data for further process estimation calculations made in section 4.4.

4.2 Observing Particle Interactions with the Melt Pool

By using higher magnification and sampling rates, it is possible to observe the behavior of individual powder particles as they are consumed by the melt pool. While particles occasionally pass directly below the surface of the melt without appreciably slowing, frequently they impact the surface, causing a ripple, then float along the surface before subsuming, as observed in Figure 15. The surface residence time for a small sample of 36 particles over 21 ms was measured, producing an average surface residence time of 370 μ s. Large scatter in residence times is

observed, with the lowest observed residence time at 32 μs and the largest at 1210 μs . The available data are liable to exclude residence times less than a frame ($<16 \mu\text{s}$) or longer than maximum video length ($>1,600 \mu\text{s}$) due to technological limitations of high speed videography, but do demonstrate the existence and relative time scale of the phenomena.

This scatter in observed surface residence times could partially originate from the dispersion in particle sizes – if the surface tension is large enough to resist penetration on initial impact, then the eventual absorption would require the particle to melt. The time to melt would depend strongly on many factors, but in particular on the mass of the particle. Heat is accumulated in the particle through both conductive/convective heat transfer from melt pool, as well as radiative heat transfer from the laser. Both of these pathways depend on the exposed surface area, a function of r^2 , while particle mass is a function of r^3 , suggesting an expected dependence of residence time on particle size.

In addition to particles floating on the surface of the melt pool, particles also freeze to the bottom of the melt pool, as observed in Figure 16. This is identifiable by the sudden halt of particle motion, instead of drifting along the surface of the melt pool. This occurs more frequently at the edges of the pool, where the melt pool is presumably shallower and at lower temperatures. Establishing a solid state thermal connection to the bottom of the melt pool would provide a pathway to dissipate incoming heat, extending the time before the particle fully melts. This corresponds with the higher frequency that these frozen particles are observed to persist beyond the length of the captured video ($>1,600 \mu\text{s}$).

4.3 Surface Roughness Formation from Particles Attached to the Surface

The existence of a residence time for particles floating on the surface of the melt pool also explains some of the differences in morphology observed in particles attached to free surfaces. In

L-DED, these attached particles constitute a primary source for surface finish nonuniformity. Beyond introducing dimensional inaccuracies, without additional surface treatment procedures these particles can detach from the final part while in service, introducing debris into the surrounding media. From Figure 16a and Figure 16c, two mechanisms are identified for particles attaching to the substrate, alongside associated cross sectional micrographs. In (a), particles float on the surface of the melt pool, providing an opportunity for the melt pool to solidify around the unmolten particle, which would be associated with the microstructure found in (b), where the original dendritic microstructure of the 316L gas atomized powder is retained, with a clear boundary retaining the spherical shape of the particle. In (c), a particle can be seen to melt and begin to vaporize as it passes through the path of the laser. This generates a molten droplet of material, which can fall back to the build and refreeze on the surface. In (d) the characteristic microstructure of this process can be seen; a fine cellular solidification pattern growing from the contact surface is observed, and the interface conforms to the original track surface.

4.4 Estimating Impact of Surface Residence Time on Mass Capture Efficiency

While interesting in its own right, the existence of a surface residence time has a further important implication for the L-DED process: floating particles can effectively shield the melt pool from accepting further particles. This is in fact observed in Figure 17a, where an incoming particle rebounds off another already floating on the melt pool surface.

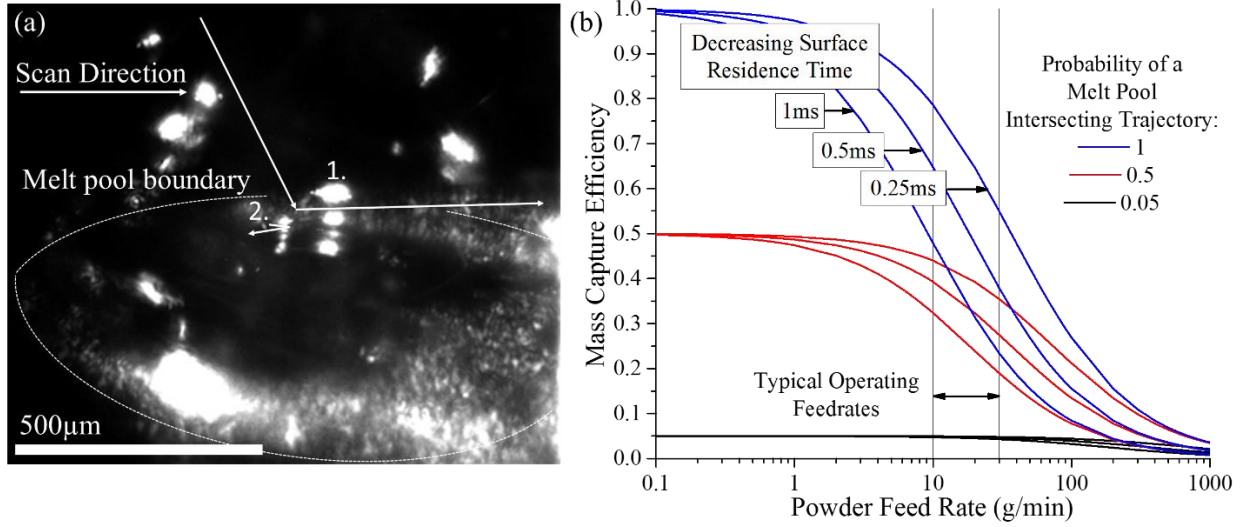


Figure 17. In (a), an incoming particle (1.) is rejected from entering the melt pool by particle already floating on the melt pool surface (2.) Video is available in the supplementary material. Rejection rates and their impact on mass capture efficiency of L-DED systems can be estimated from surface residence times and plotted over different feedrates (b). As powder efficiency increases, process sensitivity to surface residence time increases.

The consequences of this rejection mechanism can be quantified through constructing a simple relationship describing the particle loading (L) of the melt pool – here defined as the number of particles floating on the surface of the melt pool at a given time. The probability of a particle to impact an unoccupied area of the melt pool can be assumed to be proportional to the open surface area of the melt pool:

$$P_{Accept} = P_{Traj} \cdot P_{Area} = P_{Traj} \left(1 - \frac{L \cdot A_{particle}}{A_{pool} \cdot B} \right) \quad (19)$$

where P_{Int} is the probability of a sprayed particle to have a primary trajectory intersecting the melt pool area, P_{Area} is the probability of a particle impacting an open area on the melt pool, $A_{particle}$ and A_{pool} are the cross-sectional areas of individual particles and the melt pool, respectively, and B is a packing factor, here defined as a hexagonal packing factor (~ 0.907). Particle loading can then be expressed as a balance between incoming particles and particles subsuming into the melt:

$$\frac{dL}{dt} = P_{Traj} \left(1 - \frac{L \cdot A_{particle}}{A_{pool} \cdot B} \right) F - \frac{L}{\tau} \quad (20)$$

where F is the feedrate in particles per unit time and τ is the residence time of a particle on the surface of the melt pool. This equation treats particle sizes as monodisperse with uniform residence times for further calculation, but could also be numerically sampled over a desired size range and residence time spread. If steady state is achieved ($\frac{dL}{dt} = 0$), and particle loading can be solved as:

$$L = \frac{\tau \cdot P_{Traj} \cdot F \cdot A_{pool} \cdot B}{\tau \cdot P_{Traj} \cdot F \cdot A_{particle} + A_{pool} \cdot B} \quad (21)$$

This can be used to calculate the number of particles melting per second, and therefore the mass capture efficiency (ε_m):

$$\varepsilon_m = \frac{L}{\tau \cdot F} \quad (22)$$

This takes the form of a Sigmoid S-curve, as illustrated by plotting ε_m for a range of powder feedrates, surface residence times, and spray efficiencies. It can be seen that even with a perfectly collimated and focused powder stream directly feeding into the melt pool ($P_{Traj} = 1$), this particle self-shielding effect due to residence time effectively establishes an upper bound for overall process efficiency as feedrates are increased. Such a relationship implies that as machine designs move toward more powder efficient nozzle designs, the process will also become more sensitive to perturbations in surface residence time.

5. Summary

To characterize the physical interaction between particles in flight and the molten pool of metal in the L-DED process, high speed videos were recorded at 10-200 kHz under a variety of conditions. Powder particle trajectories after exiting the feed nozzles were traced to provide a statistical sample of velocity distributions under L-DED relevant conditions. Individual powder

particles were observed to impact the melt, cause a ripple, and float along the surface of the pool before subsuming below the surface of the melt pool. This surface residence time is confirmed by the distinct morphological differences between particles frozen while floating and particles that were liquified in flight and refrozen on the surface. This surface residence time of particles on the surface of the melt pool shields it from accepting further particles. A mathematical relationship was developed to illustrate how particle self-shielding ultimately limits the powder capture efficiency of the L-DED process.

CHAPTER THREE: NUMERICAL AND ANALYTICAL ANALYSIS OF PARTICLE IMPACT ON THE MELT POOL IN L-DED

Abstract

In powder based Laser-Directed Energy Deposition (L-DED), an incident laser melts a millimeter scale pool of metal, into which feedstock powder is sprayed. Previous high speed video reveals that powders are trapped by surface tension and float for a brief residence time before melting, directly contributing to surface roughness and loss of mass capture efficiency [10]. In this work, influencing factors on this behavior are investigated with numerical models through coupling a three phase (gas, liquid, solid) Computational Fluid Dynamics (CFD) model with applied surface tension to a thermal transfer model and observing the melting dynamics of an individual powder particle of stainless steel 316L. Dependence of residence time on particle size, impact velocity, melt pool and particle temperature, surface tension, and material thermophysical properties are investigated. It is found that simulations can be condensed into a simplified analytic equation, providing a rapid, explicit estimation of residence time. The demonstrated sensitivity of L-DED to powder scale surface phenomena highlights a fundamental mechanistic reason why control of feedstock powder properties is essential for reliable system behavior.

1. Introduction

1.1 Motivation

In Chapter 2, high speed video revealed that powder particles are trapped by surface tension on the melt pool surface for a period of time before fully melting. This was demonstrated to have direct consequences on the surface roughness and the mass capture efficiency of the system. However, many open questions about how this phenomenon can be mitigated or influenced remain. While high speed video is a powerful technique, the highly chaotic nature of the L-DED

powder spray means that many variables cannot be accounted for and quantified. The gas atomization process used to prepare feedstock powder produces a distribution of powder sizes, all with some degree of smaller satellite particles attached. Each of these particles will have a distinct residence time due to their unique size and morphology. Tracking individual particles and harvesting data such as particle residence time poses significant statistical and computational imaging problems. Instead, to avoid these issues and more rapidly elucidate influencing factors on the system, an impacting particle can be represented with a numerical model, which can be more readily manipulated and quantified.

1.2 Prior investigation of particle impact on liquid surfaces

Prior investigations have produced a rich history in the academic understanding of powder-liquid interactions. While explicitly useful in the present case of understanding L-DED; a much broader number of processes rely on the fundamental physics surrounding particle-liquid interactions, such as in atmospheric pollutant particle scavenging [57], wet scrubbing for industrial particulate removal [58], or even in biologically-inspired situations such as in water-strider floatation [59], [60]. While no melting or solidification occurs in these systems, many of the important findings merit review for potential relevance in the L-DED system.

The original work providing photography and analysis of solid spheres impacting fluids and causing cavitation has existed for well over a century [61], and modern interest was considerably revived by the recognition of the role of surface science on the process. Duez, C. et al. found that wettability strongly influences the dynamics of a solid body impacting a fluid, as illustrated through the formation of a ‘splash’ in non-wetting spheres (absent in wetting spheres), which is associated with the threshold velocity for formation of an air cavity behind the impacting sphere [62]. This was numerically modelled by Do-Quang, M. et al. using the Navier-Stokes

equations coupled with the Cahn-Hilliard equations [63], [64], which permitted further analysis of the relative strength of influencing factors. Lee, D.G. et al studied the impact of superhydrophobic spheres with high speed video under various solid/liquid density ratios and impact velocities, and showed that particles can penetrate into the fluid, oscillate on the surface, or even rebound [65]. Aristoff et al. studied the impact of hydrophobic steel spheres into water, and used them to predict cavity shapes and impact depths for low Bond number impacts in quasi-static and high-speed scenarios[66]. Liu, D. et al. studied penetration of hydrophilic glass beads with high speed video and developed a model for critical impact velocity for penetration into the fluid [67]. Lee, D.G. and Kim, H.Y. also developed a model to add viscous effects on a particle sinking into a fluid using the steady state solution to the Stokes equation [68].

Wang, A et al. developed an in-situ high speed video system to improve measurement of submillimeter impacts for individual particles [69], which demonstrate significantly different behavior than mm to cm sized spheres. This led to recognition of the importance of using a dynamic contact angle by Wang, A. et al., who developed criteria for predicting if a hydrophobic, micron sized particle will rebound, penetrate, or oscillate on a liquid surface based on a dynamic model that captures effects from pinning and sliding of the contact line around the surface of the particle[58]. Further study of micron-scale particles was produced by Kintea, D.M. et al. who used numerical simulations to study impacts of rotating spheres and spheres impacting at an angle, and found that the Weber number, density ratio, and wettability were dominating influences, with capillary forces dominating for small particles [70]. Numerical modelling of micron-sized particles was performed by Ji, B. et al which similarly found particles would penetrate or oscillate on the surface depending on wettability and the hydrodynamics of the fluid as kinetic energy is exchanged [71].

Through these and other experimental and modelling studies, several important behavioral regimes are established. First, there is a critical velocity for a particle to penetrate past the surface and continue to sink after the fluid has closed in behind it. This depends on whether the initial kinetic energy of the particle is larger than the work done by surface tension submerging the particle. From Wang [58], these quantities are:

$$E_k = \frac{2}{3} \pi R^3 \rho_s v_0^2 \quad (23)$$

$$W_{sink} = 2\pi R^2 \sigma \left\{ \frac{1}{2} A \sin^2 \phi_0 \sin^2(\phi_0 + \theta_a) - \frac{2}{3} \sin^3 \frac{\phi_0}{2} \left[3 \sin\left(\frac{\phi_0}{2} + \theta_a\right) + \sin\left(\frac{3}{2} \phi_0 + \theta_a\right) \right] \right\} \quad (24)$$

where R is the particle radius, σ is the fluid's surface tension, θ_a and θ_r are the advancing and receding contact angles, and ϕ_0 is the angular position of the contact line at the moment of reversion when particle velocity drops to zero. $A = \ln(2.5/Bo) - \varepsilon$, where ε is the Euler constant, and Bo is the Bond number $Bo = \Delta \rho g l^2 / \sigma$. When $W_{sink} < E_k$, the particle will penetrate into the fluid and continue to sink.

Non-penetrating particles can either be pinned by surface tension and oscillate on the surface until viscous damping attenuates motion, or under certain conditions, actually rebound from the fluid. From Wang, this threshold can be estimated by comparing the work done by surface tension as the particle moves from its lowest point ϕ_0 to a position fully removed from the fluid surface ($\phi = 0$). Work is done piecewise, as the contact line is pinned in place on the particle when $\theta_a > \theta > \theta_r$, and the meniscus takes a different shape as the contact line is receding $\theta = \theta_r$. From this, Wang obtains:

$$\begin{aligned}
W_{re} = & \pi \sigma R^2 A \sin^2 \phi_0 [\sin^2(\phi_0 + \theta_a) - \sin^2(\phi_0 + \theta_r)] \\
& - \frac{1}{6} \pi R^2 \sigma \left[-3A(\cos(2\phi_0 + \theta_a) - 2 \cos \theta_r \right. \\
& \left. - 1) \cos^2 \left(\phi_0 + \frac{\theta_r}{2} \right) - 3 \cos(\phi_0 - \theta_r) - 6 \cos(\phi_0 + \theta_r) \right. \\
& \left. + \cos(3\phi_0 + \theta_r) - 5 \sin \left(\frac{\theta_r}{2} \right) + 3 \sin \left(\frac{3\theta_r}{2} \right) \right]
\end{aligned} \tag{25}$$

For $W_{re} > 0$, particles will rebound; for $W_{re} < 0$, particles will be trapped by surface tension and oscillate on the surface. These regime thresholds are plotted in an excerpt from [58]:

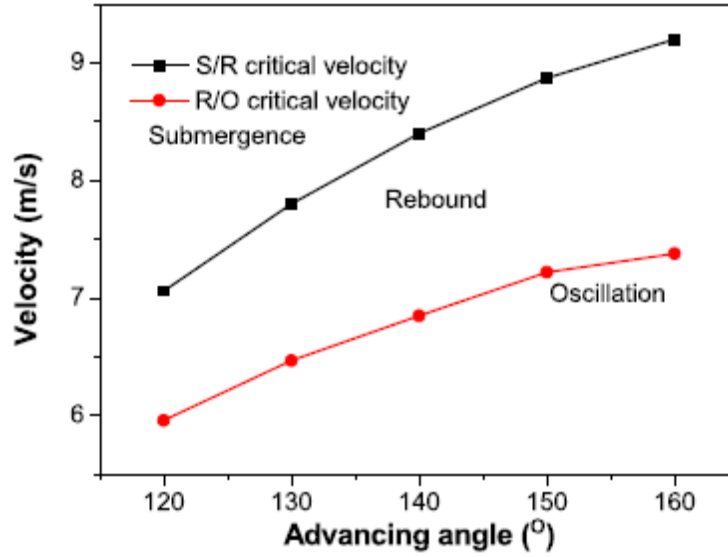


Figure 18. Predicted regimes for particle submergence, rebound, or oscillation for a PMMA particle on water as a function of incident velocity and advancing contact angle, from Eqn (23)-(25) [58]. Reprinted with permission from Elsevier and Q. Song.

For particles that penetrate into the fluid, there is an additional threshold that determines whether or not a vapor cavity will form behind the sphere, which depends on the wettability of the particle, and the incoming velocity of the particle. This is estimated by Duez et al. [62].

1.3 Wettability of metals and oxides at high temperature

While surface tension and energy values are relatively well known for water and PMMA with various surface treatments at room temperature, the situation in a metal AM system is dramatically complicated when considering that the system operates at high temperature with

metal alloys with difficult to quantify degrees of oxidation. Many studies have been performed using many methods measuring surface tensions of liquid metals for both elemental and some alloy systems [72], and results have been shown to depend strongly on the technique used and the control of surface active elements such as oxygen and sulfur. The literature is here reviewed to couch the proposed model in terms of the availability of relevant data and reasonable expectations of the accuracy of this data.

Four commonly employed methods are used to determine surface tension. In the sessile drop (SD) technique the advancing and retreating contact angles between a molten droplet and a substrate are measured via goniometer. In the maximum bubble pressure method (MBP) a capillary is submerged in a liquid melt and inert gas flowed into the melt; the pressure at the point of breakoff of the bubble from the capillary is related to not only the hydrostatic pressure of the liquid but also to the pressure resisting collapse of the curvature of the interface. This has the advantage of generating new surface area for each bubble, reducing the influence of surface-active elements. The electromagnetic levitation (EML) technique uses an inductive AC coil and eddy currents to heat and levitate a droplet of molten metal; from the frequency of the oscillation of the droplet the surface tension can be determined. This has the advantage of being vessel-free, and has no interaction with a solid supporting surface. Finally, for very refractive elements the pendulum droplet technique can be used, where the tip of a wire is melted by an electron beam; the maximum size of a pendulum droplet that forms is related to its surface tension.

Using these four methods, studies have determined the relationship between temperature and surface tension. For a completely pure elemental metal, the surface tension decreases linearly with temperature as the excess free energy difference between liquid and gas phases drop. However, in all applications some finite degree of sulfur and oxygen and other surface-active

elements are present in the metal and in the atmosphere. As described by the Butler equation [73] these preferentially migrate to the surface where they are more energetically stable, which reduces surface tension. As temperature rises, the increased entropy of the system rebalances the equilibrium concentration of the surface concentration for these elements, forcing them away from the interface and increasing surface tension. This effect can even flip the sign of the temperature dependence of surface tension $\left(\frac{d\sigma}{dT}\right)$ to be positive for high enough concentrations [74]. This is particularly relevant to the welding and AM communities as the thermocapillary effect is a dominant source of convective flow in the melt pool; if $\frac{d\sigma}{dT} < 0$ then flow on the surface will tend to move outward away from the hottest point in the center of the pool, with the converse being true if $\frac{d\sigma}{dT} > 0$ [5].

While the welding and AM literature is aware of the shaping influences of liquid surface tension and its dependencies on the process, the current study is focused on the interaction between powder particles and the melt pool. This involves two new terms to determine contact angle behavior: the surface energy of the solid particles vs the vapor phase and the surface energy between the solid particles and the liquid melt. While there are complex theoretical models describing the surface energies of solids based on thermodynamic integration, molecular dynamics or density functional theory [75], it is experimentally very difficult to measure these values. Two methods used are zero-creep method and the multiphase equilibrium technique, which are reviewed in [76], which also reports some observed values for elemental systems.

Further complicating the issue, all metal powders have some degree of oxidation when exposed to atmosphere or an imperfect vacuum. This oxidation layer can provide much of the corrosion and oxidation protection for an alloy system, but can be expected to modify the surface energies and wettability of the particle. Some values for contact angles of elemental metals on

different oxides are reviewed by Eustathopoulos [76]; perhaps the most relevant value reported to the present system is for liquid iron and Cr_2O_3 of 89° , which would be the oxide that passively stabilizes a stainless surface. As the particle melts however, this oxide layer presumably also dissolves into the melt, possibly dynamically modifying the wettability towards that of the liquid on the pure metal over time. Oxide layers can frequently be rough and featured at the micro level, which has the known effect on wettability of increasing disparity between advancing and retreating angles.

Reviewing the information in the literature demonstrates that experimental and theoretical challenges in obtaining system specific surface energies pose a serious barrier to obtaining quantitative values for use in the model. The influences of local temperature, bulk and contaminant concentration, oxide phase formation and surface roughness would all serve to further complicate and obfuscate these surface energy values. Given these issues, it becomes apparent that any model of particle wettability for metallic systems would be incomplete without probing particles over a range of different wettability values. In the presented model, contact angle was set to a variety of values and the key results monitored; this not only insulates the study from sensitivity to the unknowns inherited from wettability measurements, but it also provides feedback on if surface treatments intended to modify wettability will influence the overall process behavior. The implementation and findings of this are discussed in following sections.

1.4 Summary

From reviewing the information available, it becomes clear that a knowledge gap in the AM literature exists regarding the interactions of individual powder particles as they are acted on by surface tension forces. Many basic questions remain unanswered; such as what influencing factors control the contact area between the particle and the melt pool, or if particles melt primarily

from incident laser energy or thermal conduction from the melt pool. It is the aim of this study to apply and expand numerical and analytical techniques used in prior literature to answer these questions and provide a realistic assessment of how the large range of sizes and morphologies present in a real powder feedstock influence the residence time, probability of capture, and the surface roughness of the deposited part.

2. Numerical Methods

To characterize the floating and melting behavior of particles on the surface of the melt pool, a single particle was simulated with the Volume of Fluid Method in commercial software COMSOL Multiphysics®. The modeled particle was spherical and free of spin, permitting an axisymmetric reduction of the computational domain to a 2D problem. The particle and melt pool boundaries were tracked via the phase field method, with three phases (solid: $\phi_A = 1$, $\phi_B = 0$; liquid: $\phi_A = 0$, $\phi_B = 1$; gas: ϕ_A , $\phi_B = 0$). Surface tension was implemented via the Cahn-Hilliard equations as implemented in COMSOL®.

In order to reduce computational load, three separate fidelities of model were executed, with the lowest fidelity, least computationally expensive model run for a full factorial expansion of the design levels (Table 7), the medium fidelity model run for the baseline case and five parameter sweeps, where all variables were maintained at the baseline case except for the swept parameter, and a high fidelity model run for only the baseline case. It was found that temperature dependent material properties introduced significant instabilities for lower fidelity models, so two sets of properties were used for different model fidelities as specified in Table 8, Table 9, Table 10, and Table 11. Stainless steel 316L and other parameters were chosen to most closely correspond to conditions used in previous high speed video experiments [10]. Initial particle velocity was set to 4 m/s.

For the high and medium fidelity models, boundary conditions were no-slip, closed, and thermally insulating on the outer perimeter boundary (as diagrammed in Figure 19b). On the top and bottom boundaries temperature was fixed to ambient and the melt pool temperature respectively. Heat flux into the particle from the incident laser can be estimated from the laser intensity, the particles surface emissivity, and the particles cross section, so instead of including this directly in the numerical model the heat transport from the two mechanisms of conduction from the melt pool and radiation can instead be directly compared to each other to find the dominant mode, as discussed in following sections.

For the low fidelity models, no phase field or fluid flow calculations were executed, and instead the particle was stationary. For a particle with low mass on a fluid of high surface tension, as in the present case, the weight of the particle will impose minimal deformation of the fluid meniscus, so here it is neglected and the particle's height is set so the defined contact angle is at the equilibrium contact angle with a flat fluid surface.

Table 7. Design of Experiment (DOE) levels for numerical models.

<i>Model Parameter</i>	Baseline	Levels	Units
<i>Particle Radius (r_{part})</i>	40	5, 10, 20, 40, 80*, 160*	μm
<i>Initial particle temperature</i>	20	20, 100, 200, 400, 800	$^{\circ}\text{C}$
<i>Initial melt pool temperature</i>	1900	1550, 1600, 1700, 1800, 1900, 2000	$^{\circ}\text{C}$
<i>Equilibrium Contact Angle (θ_E)</i>	127	1, 114, 117, 123, 126, 131, 138, 143; * 20, 45, 90, 135, 160	(deg)

*Low fidelity only

Table 8. Hierarchy of models executed trading off accuracy for computational speed.

<i>Fidelity</i>	DOE	Temperature Dependent Properties (Table 9)	Temperature Independent Properties (Table 10)	Not Included	Description
<i>High</i>	Baseline only	ρ, μ, k	C_p, T_l, T_s, H_{fus}	-	Adaptive mesh
<i>Medium</i>	Parametric sweep	-	$\rho, \mu, k, C_p, T_l, T_s, H_{fus}$	-	Coarser mesh, lower solid viscosity
<i>Low</i>	Full factorial	k	C_p, T_l, T_s, H_{fus}	$\rho, \mu,$	No fluid flow, thermal field at equilibrium contact only
<i>Analytic</i>	Full factorial	-	k, C_p, T_l, T_s	ρ, μ, H_{fus}	Infinitely small particle, conduction only

Table 9. Thermally dependent 316L stainless steel material properties used for higher fidelity models.

<i>Property</i>	Solid	Liquid	Gas	Units	Phase Dependency Relationship
<i>Density</i> (ρ)	$-0.5132T + 8121.2^*$	$-0.7729T + 8212.6^*$	1.6^\dagger [77]	Kg/m ³	$\max(\varphi_A \cdot \rho_s + \varphi_B \cdot \rho_l, \rho_g)$
<i>Viscosity</i> (μ)	$1e6^{\dagger\dagger}$	$0.3699 \cdot \exp\left(41.4 \frac{KJ}{mol} \cdot \frac{T}{R}\right)^\ddagger$ [78]	$1.8e-2^\dagger$ [77]	mPa·s	$\max\left(\text{sig}\left((\varphi_A - 0.5)\beta_\mu\right) \cdot \mu_s + \text{sig}\left((\varphi_B - 0.5)\beta_\mu\right) \cdot \mu_l, \mu_g\right)$
<i>Thermal Cond. (k)</i>	$0.0136T + 11.44^*$	$0.0129T + 6.4881^*$	0.0172^\dagger [77]	$\frac{W}{m \cdot K}$	$\max(\varphi_A \cdot k_s + \varphi_B \cdot k_l, k_g)$

*Linear approximation of [43][†]Left as constant at 20°C[‡]For liquid Fe^{††}Intentionally unphysical for stability

Table 10. Thermally independent 316L stainless steel material properties used for lower fidelity models.

Property	Solid	Liquid	Gas	Units	Phase Dependency Relationship
<i>Density</i> (ρ)	7950 [‡]	6881 [†]	70 ^{††}	Kg/m ³	$\max(\varphi_A \cdot \rho_s + \varphi_B \cdot \rho_l, \rho_g)$
<i>Viscosity</i> (μ)	1e3 ^{††}	1 ^{††}	3e-2 ^{††}	mPa·s	$\max\left(\text{sig}\left((\varphi_A - 0.5)\beta_\mu\right) \cdot \mu_s + \text{sig}\left((\varphi_B - 0.5)\beta_\mu\right) \cdot \mu_l, \mu_g\right)$
<i>Thermal Cond.</i> (k)	21 [*]	28.5 [†]	0.00001 ^{††}	W/(m·K)	$\max(\varphi_A \cdot k_s + \varphi_B \cdot k_l, k_g)$
<i>Specific Heat</i> (C_p)	6082 (0-T _m)	8011 (T _m -T _v)	1 ^{††} (T _v -T _∞)	J/(kg·K)	$\max\left(\left(C_p + \frac{d}{dT}H_{fus}(T)\right) \cdot (\varphi_A + \varphi_B), 1\right)$

^{*}Average of [43] from ambient to T_m [†]Left as constant at T_m
[‡]Left as constant from 25C ^{††}Intentionally unphysical for stability§

Table 11. Other SS 316L thermophysical properties used.

Property	Value	Units	Temperature Relationship	Source
<i>Liquidus Temp</i>	1454	°C	-	[43]
<i>Solidus Temp</i>	1400	°C	-	[43]
<i>Enthalpy of fusion</i> $H_{fus}(T)$	2.61e5	J/kg	$H_{fus}(T) = H_{fus} \cdot \text{step}(T - T_m, T_{liquidus} - T_{solidus})$	[43]
<i>Liquid-Vapor Surface Tension</i> (σ_{LV})	σ_{refLV} : 1.34 σ_{TLV} : 4.6×10 ⁻⁴	N m ⁻¹ N m ⁻¹ K ⁻¹	$\sigma_{LV} = \sigma_{refLV} + T \sigma_{TLV}$ $T_{ref} = 1450^\circ\text{C}$	[72]

The model uses a secondary sigmoid function for determining viscosity in order to affect a sharper boundary between phases:

$$\text{sig}\left((\varphi_A - 0.5)\beta_\mu\right) = \left(\frac{1}{1 + \exp(-(\varphi_A - 0.5)\beta_\mu)}\right) \quad (26)$$

The phase boundary size can be tuned with the β_μ parameter independently of the boundary used for other properties. This is useful as the normal phase field smoothing function extends the relatively high viscosity of the solid far into the gas phase, which effectively expands the particle radius and interferes with appropriate wetting of the particle. Additionally, a maximum operator

is used on the viscosity, density, thermal conductivity and specific heat in order to encourage solution stability and prevent values dropping below zero.

In the model, the melting phenomenon is simulated by converting φ_A to φ_B at the solid liquid interface when temperature exceeds the specified melting point. This is implemented through introducing a weak form equation:

$$0 = \int_{\Omega} (\varphi_A^4 \cdot \varphi_B^4) \cdot \frac{1}{1 + \exp\left(\frac{T_{\text{melt}} - T}{\beta}\right)} \cdot \alpha \cdot dS \quad (27)$$

where the term $\varphi_A^4 \cdot \varphi_B^4$ confines the influence of the equation to the solid-liquid interface, and the second term is a logistic function that activates at T_{melt} . The β parameter governs the temperature range over which the transition occurs (spreading phase conversion to the liquidus and solidus temperatures), and α is a scaling parameter.

In order to reduce computational load and permit higher resolution of the phase boundary for the high-fidelity model, an adaptive mesh scheme was implemented with the COMOSL® algorithm. This refined elements along the phase boundaries by splitting the longest edge of each element in the target area up to six times until the maximum number of refined elements allowed was reached (set to 300% of the original element count). The algorithm targeted the phase boundaries using a scalar refinement factor (R):

$$R = \phi_A^2 \phi_B^2 + \phi_A^2 \phi_C^2 + \phi_B^2 \phi_C^2 \quad (28)$$

The Cahn-Hilliard equations are widely used due to their ability to conserve mass globally and their flexible formulation; however, using them for small spherical droplets of material poses a special challenge as droplets with high curvature can spontaneously shrink and lose phase fraction to surrounding media as the solver minimizes energy [79]. Two methods exist to combat this undesired artifact, first, under conditions where the droplet is large compared to the entire

domain of the simulation there exists a critical radius below which the droplet will not shrink. This occurs as surrounding media becomes saturated with the droplet's lost phase fraction, providing a local energetic minimum preventing further shrinkage. The second method is to choose the mobility parameter to be sufficiently small to limit phase loss into the surrounding media. In the present simulation, the choice of particle and domain size is driven by mimicking real machine conditions, and it is not practical to establish the energetic minima to prevent shrinkage; so instead the mobility parameter is tuned to mitigate shrinkage. Mobility (γ) is set to approximately $1e-10$ m³/s along the phase boundaries for the baseline simulation, and is scaled for different simulations according to the proportions proposed in [79]:

$$\gamma \sim \frac{r\epsilon^2}{\sigma t_{sim}} \quad (29)$$

where t_{sim} is the total time the simulation is run, r is particle radius, σ is surface tension, and ϵ is the interface thickness parameter, which is tuned to $\epsilon = 25 \frac{l}{2}$, where l is the refined element size, which was found to provide at least eight elements across each phase interface after adaptive refinement.

3. Results

3.1 Baseline Simulation Results

A timeline of the thermal and phase field evolution of the 'baseline' case for each fidelity of model is shown in Figure 19, with a three-dimensional representation in Figure 20. Parameters used for the baseline case can be found in Table 7. As can be seen, the model successfully predicts particle capture by surface tension and melting through conduction. The initial kinetic energy of the particle is imparted to the molten steel, creating a ripple which travels to the outer edge of the modelled domain. After the particle has been heated by thermal conduction with the melt pool to

the solidus temperature, it begins to melt, using the thermal field to adjust the phase composition along the interface, as enforced by the weak form Equation (27).

Even in the absence of particle penetration below the melt pool surface, high impact velocity has a secondary effect in inducing a ripple in the molten metal. As a closed boundary was used for the outer domain of the simulation, the ripple induced by the particle impact rebounds and continues to perturb the fluid for a period of time before the ripple is damped by viscous effects. This ripple is observed in high speed video in [10], however, the ripple does not continue to rebound and move the particle as the melt pool boundaries are significantly wider than the current simulation domain. As the ripple adjusts the degree of thermal contact between the particle and the liquid, it can be expected to influence the absolute rate of heat transfer into the particle. This is apparent from the oscillations in heat accumulation in Figure 22. Such particle motion tends to have the effect of disperse particle residence times, as heat transfer depends on the peculiarities of fluid flow for a given particle size and impact velocity.

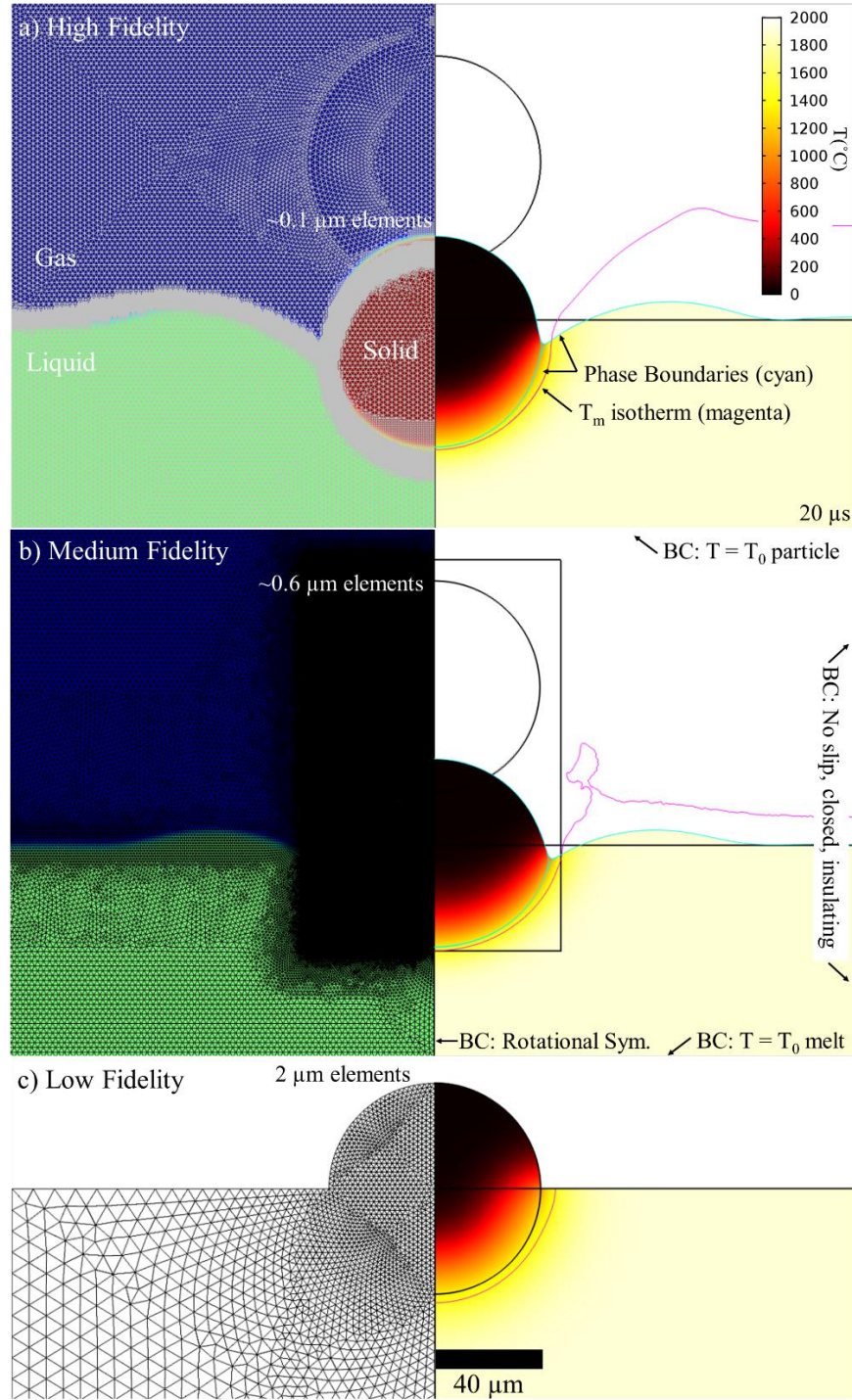


Figure 19. Comparison of model fidelities, including mesh (left), phase field (left side color), and thermal field (right side color scale), for each simulation at $20\ \mu\text{s}$. The high-fidelity model in a) used an adaptive meshing technique to refine phase boundaries, allowing for a sharper interface and higher solid viscosities. In b), the medium fidelity model used a coarser mesh to permit more parameter combinations, but some resolution of the interface was lost, which required lower solid viscosity for convergence, which allowed some deformation of the particle. In c), the low fidelity model only calculates thermal conduction for particles assumed to be stationary at the equilibrium wetting position (neglecting meniscus deformation for low mass particles).

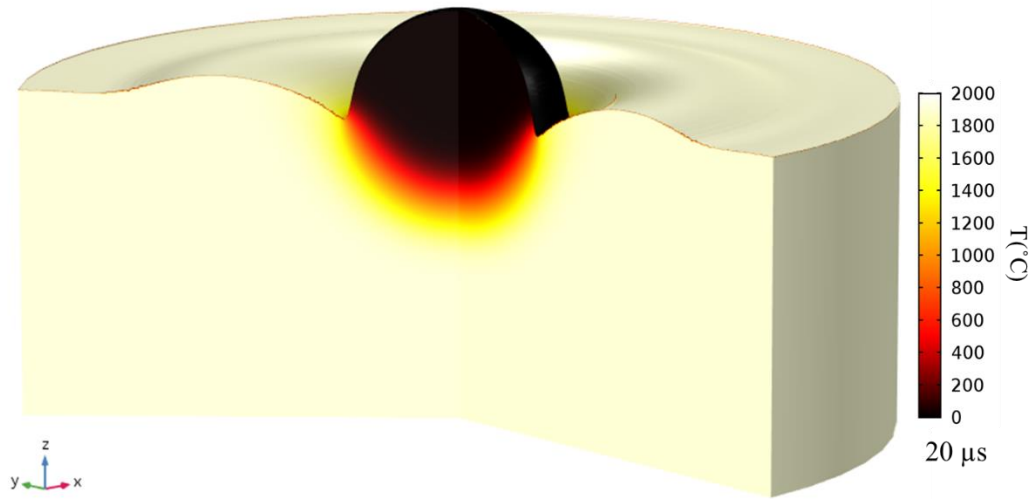


Figure 20. 3D rendering of the thermal field of the baseline high-fidelity model for solid and liquid phases, at 20 μs .

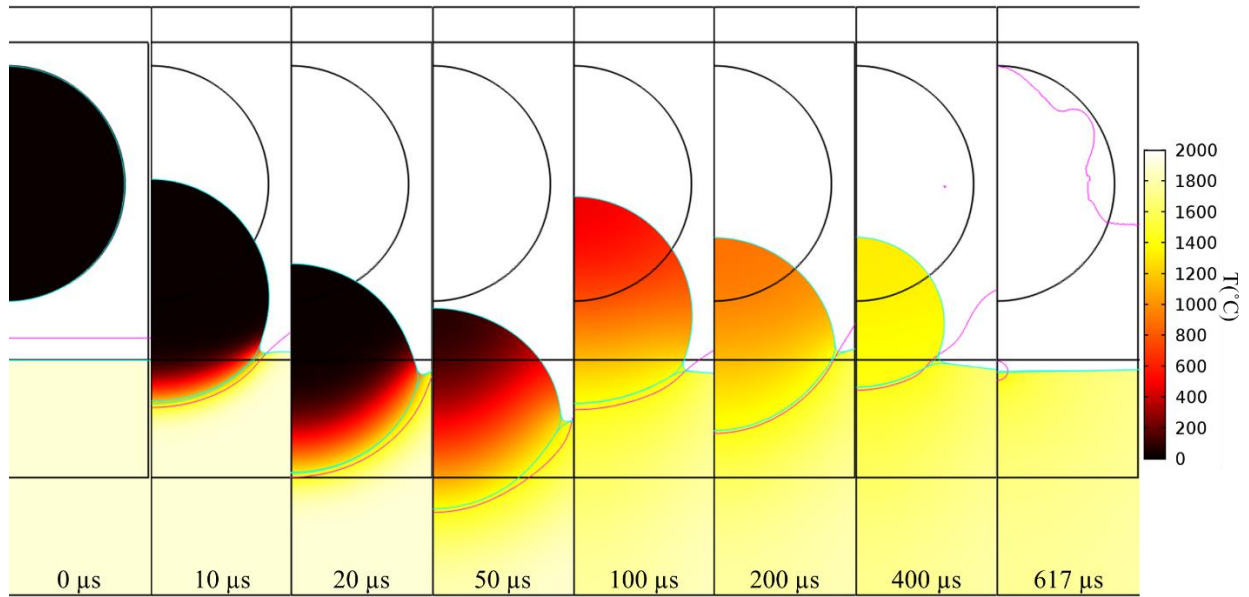


Figure 21. Time series of particle impact using medium fidelity at baseline parameter settings. Particle is captured by surface tension and oscillates before fully melting at 617 μs . The outer portion of the fluid computational domain is truncated for particle visibility.

Heat transfer into the particle is not explicitly tracked by the model, as the phase boundary migrates over time, so instead total heat absorbed by the particle was instead extracted by adding

two components: heat added to the particle to raise its temperature, and heat used to overcome latent heat of fusion. Heat added to raise the temperature must account for the rise in internal energy for both the solid particle and mass already lost to the melt, as expressed in the first two terms in Equation (30). Latent heat (H_{fus}) is accounted for in the third term:

$$H_{Total} = \Delta H_{solid} + \Delta m C_p (T_m - T_{0part}) + \Delta m H_{fus} \quad (30)$$

where ΔH_{solid} is internal energy integrated by COMSOL[®] over the solid phase domain, and Δm is the mass loss of the particle. The accumulation of the components of heat transfer are plotted for the baseline simulation in Figure 22.

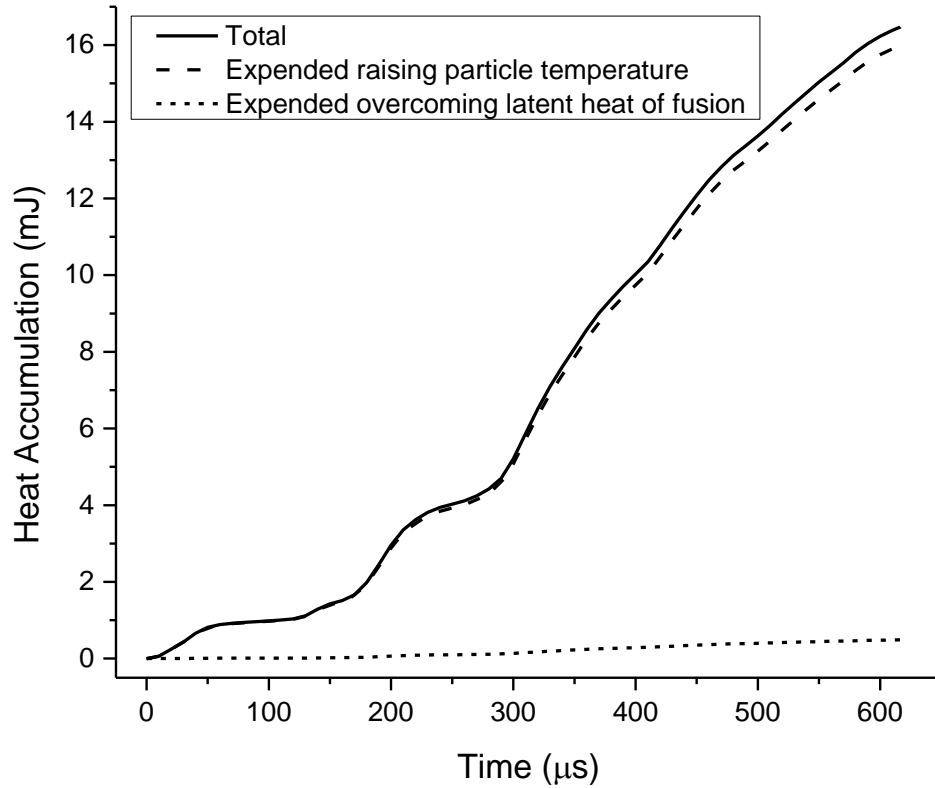


Figure 22. Heat accumulated in the particle for the baseline settings for the medium fidelity simulation, accounting for mass loss of the particle over time. First particle impact is at 5μs. Transient wetting modulates heat transfer into the particle as it oscillates up and down on the melt pool surface.

3.2 Parametric Variation of Impact Velocity, Particle Diameter, Particle Temperature, Melt Pool Temperature, and Wettability

As may be intuitively expected, particle residence time strongly depends on all factors that modify heat exchange between the particle and the melt pool, as shown in Figure 23 from the medium fidelity model parameter sweeps. Increasing the superheat of the melt pool generates a stronger thermal gradient, which reduces the amount of time required for the particle to melt. Increasing the particle's initial temperature or decreasing particle mass decreases the total heat required melt it, which lowers residence time. Lower contact angles with higher wettability promote thermal transfer between the melt pool and the particle, reducing residence time. At high contact angles (low wettabilities), the particle was actually ejected from the fluid surface by the returning ripple, which is discussed further in section 4.3.

While parameters for the baseline model presented were chosen in an attempt to represent the average case for a real L-DED system, conditions can vary quite strongly away from any particular average value, for instance, particle sizes will always show some dispersion due to the nature of the gas atomization process. Additionally, some variables of the system are not easily measured, such as the wettability of molten metals on particle surfaces with variable degrees of oxidation, surface roughness, and adsorbed moisture. One advantage of using a numerical model is that these parameters can be adjusted independently to gain a sense of their relative importance in controlling system behavior.

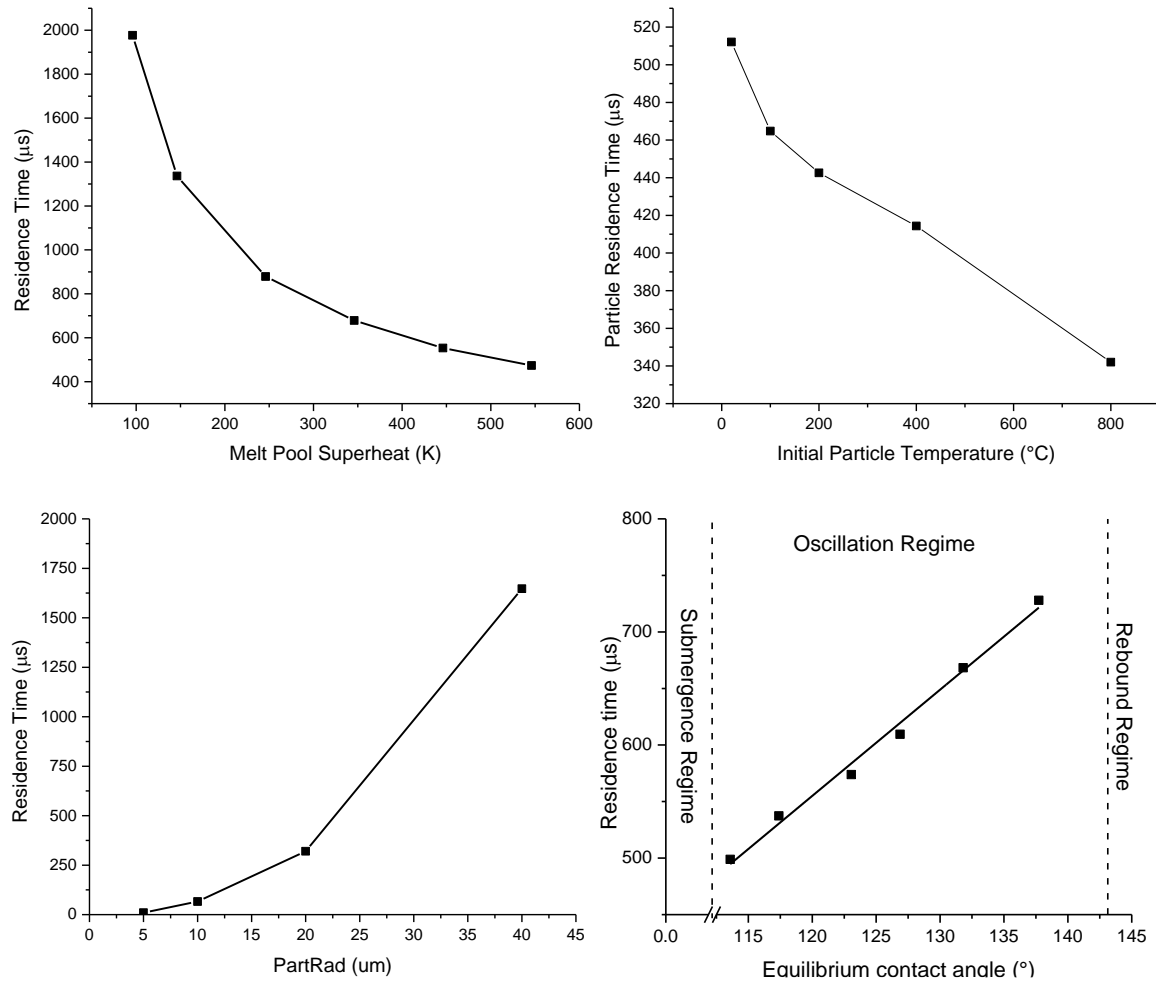


Figure 23. Influencing factors on particle residence time, the length time between initial particle impact and full melting. All factors were held constant at the ‘baseline’ settings (Table 7-Table 11) except for the plotted variable. In the fourth panel, an equilibrium contact angle of 143° resulted in a rebounding particle, and a contact angle of 1° resulted in complete penetration, as shown in Figure 26.

4. Discussion

While the relationships apparent from Figure 23 already represent a step forward in the AM literature in understanding discrete particle behavior while impacting the melt pool, further analysis can open new insight into L-DED. In section 4.1, a classic analytic solution to heat transfer in spherical coordinates is used to establish power dependencies of key parameters. In Section 4.2, sources of heat accumulation in the particle are compared and a criterion is proposed to determine

dominant melting modes. In section 4.3, issues surrounding determination and effects of surface wettability are explained.

4.1 Analytic Estimation of Particle Residence Time

While the present numerical model provides great advantages in accurately exploring complex particle behaviors, it is also of great practical use to use them as a benchmark to assess the accuracy of a simplified analytic representation. This could provide future work with a rapid estimate for particle behavior in less well studied material conditions. If it is assumed that particle melting depends most strongly on heat conduction from the surrounding fluid and fluid convection is slow relative to melting, one can treat the particle as a point heat sink in a hemi-spherically symmetric infinite domain, and apply classic diffusion equation solutions [80]:

$$\frac{dT}{dt} = \alpha \nabla^2 T \quad (31)$$

$$T_0 = T_{0,pool} - T_{0,part} \delta(r) \quad (32)$$

where $T_{0,pool}$ and $T_{0,part}$ are the initial temperatures of the molten fluid and the particle respectively, r is radial distance, and $\delta()$ is the Dirac delta function. The point heat sink is calculated from the mass and thermal properties of the particle:

$$\Delta U_{part} = \frac{4}{3} \pi r_p^3 \rho C_p (T_{0,pool} - T_{0,part}) \quad (33)$$

where ρ and C_p are density and heat capacity of the particle respectively. This has an exact analytic solution:

$$T(r, t) = T_{0,pool} - 2 \frac{\Delta U_{part}}{\rho C_p} \frac{1}{(4\pi t \alpha)^{\frac{3}{2}}} \exp\left(-\frac{r^2}{4\alpha t}\right) \quad (34)$$

where α is thermal diffusivity in the fluid and t is time. The extra factor of 2 reflects that heat is dissipating only semi-spherically below the particle.

This treatment neglects a great deal, including latent heat of fusion, wettability of the particle, fluid convection, particle oscillation and wettability effects, and temperature dependence of material properties. However, it is easy to obtain and can provide insight into the expected scaling of factors that influence particle melting times. Setting $T = T_m$ and evaluating at $r = 0$ allows us to obtain an explicit formula for particle residence time:

$$t_{melt} = \frac{1}{4\pi\alpha} \left(\frac{8}{3} \pi r_p^3 \frac{T_{0,pool} - T_{0,part}}{T_{0,pool} - T_m} \right)^{\frac{2}{3}} \quad (35)$$

The predictions of this formula are compared to numerical simulation in Figure 24a). It is apparent that the neglected wettability of the particle strongly shifts residence time behavior from the dispersion between simulations with different equilibrium contact angles. To account for this, an improved analytic solution that separates the particle and melt into distinct domains may be possible, but is not solved here. Instead, a prefactor that scales with equilibrium contact angle is applied to (35):

$$t_{melt,corrected} = 10^{-(A\theta_E+B)} t_{melt} \quad (36)$$

where A and B must be empirically determined. While mathematically crude, this neatly collapses the differences between numerical and analytical predictions, as seen in Figure 24b), which suggests the form that an improved analytic approach might take. Logarithmic plotting tends to visually suppress error and heteroscedasticity, for Figure 24b) all analytic predictions fell within $\pm 50\%$ of the respective numerical prediction. This variation can be attributed to the limitations of the assumptions made in the analytic model, some of which may be improved upon in future work. This demonstrates that the analytic model is able to capture the broad sweeping power relationships, but is still a first order approximation that requires grounding with more detailed numerical modelling or experiments.

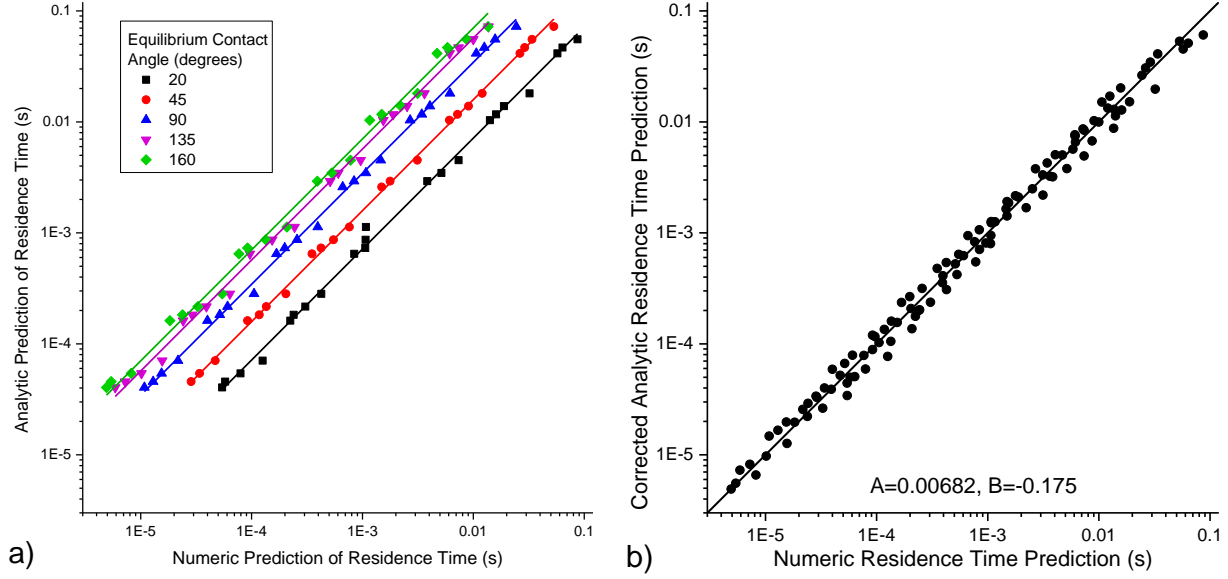


Figure 24. Comparison of direct analytic estimation and FVM numerical modelling of particle residence time. The analytic model treats the particle as a point, so wettability and contact with the melt pool is not accounted for, as seen from the large systematic error present in a). In b), a fitting prefactor has been applied that depends on the contact angle per Equation (36), which collapses the prediction curves while preserving temperature and particle size relationships.

4.2 Dominant Modes of Particle Heat Accumulation

Thermal transfer between the melt pool and the particle can be seen to be modulated by transient wetting in Figure 22. As the particle oscillates the triple point advances and retreats, which changes the constraining contact area between particle and fluid. The rate of particle heat accumulation can be seen to fluctuate with this changing thermal contact.

While the numerical model accounts for thermal conduction and convection in the particle and melt pool, some floating particles will also absorb energy from the laser. The contribution of incident laser energy to the powder particle can be readily estimated from the cross-sectional area of the powder particle, the spectral absorptivity of the particle ϵ , and the intensity of the laser I :

$$q_{laser} = \epsilon I \pi r_{part}^2 \quad (37)$$

For instance, for an arbitrary set of operating conditions with SS316L powder with a 40 μm radius, emissivity of 0.35, and laser intensity of $5.1\text{e}8 \text{ W/m}^2$ (400 W focused to 1mm beam

diameter), the power delivered would be ~ 0.9 W, which would melt the particle in ~ 20 ms. This is over an order of magnitude longer than the simulated baseline in the numerical model, even for lower melt pool superheats (Figure 23c). The amount of energy required to melt the particle scales with r_{part}^3 , while the energy provided by the laser scales with r_{part}^2 , implying that direct heating by the laser may be more significant at lower particle sizes. To judge this, residence times are plotted against the numerical model for conduction in Figure 25. It can be seen that even if a particle is exposed to the laser in flight, (estimating for a relatively slow particle flying over the melt pool at a 60 degree angle: $2 \text{ ms} = 1 \text{ mm} / \cos(60^\circ) / (1 \text{ m/s})$) the dominant heat transport mechanism will be conduction.

Naturally, this situation changes for different material systems and machine setups; one may expect the particles to pick up more relative energy from the laser if they have a higher emissivity, a longer flight time, or conduction from the melt pool is lowered. Laser intensity varies spatially over the surface of the melt pool, and can be much higher than this estimate if the beam is focused, which changes this relationship. If the laser is focused to a 0.25 mm beam diameter, a factor of 4, beam intensity increases by a factor of 16, which out competes thermal conduction for 40 μm particles for our arbitrarily picked scenario. However, focusing the laser would contract it away from the boundary of the melt pool, leaving the perimeter unirradiated and relying on conduction alone to melt particles. Additionally, as intensity increases, the melt pool will enter the ‘keyhole’ mode regime, where back pressure from vaporized metal causes a cavity to form [9], which will interact with individual powder particles in very different ways than the simulation presented. However, for all these scenarios, one can reasonably expect the melt pool residence time to depend strongly on factors outlined by Equation (36) that govern conduction from the melt pool.

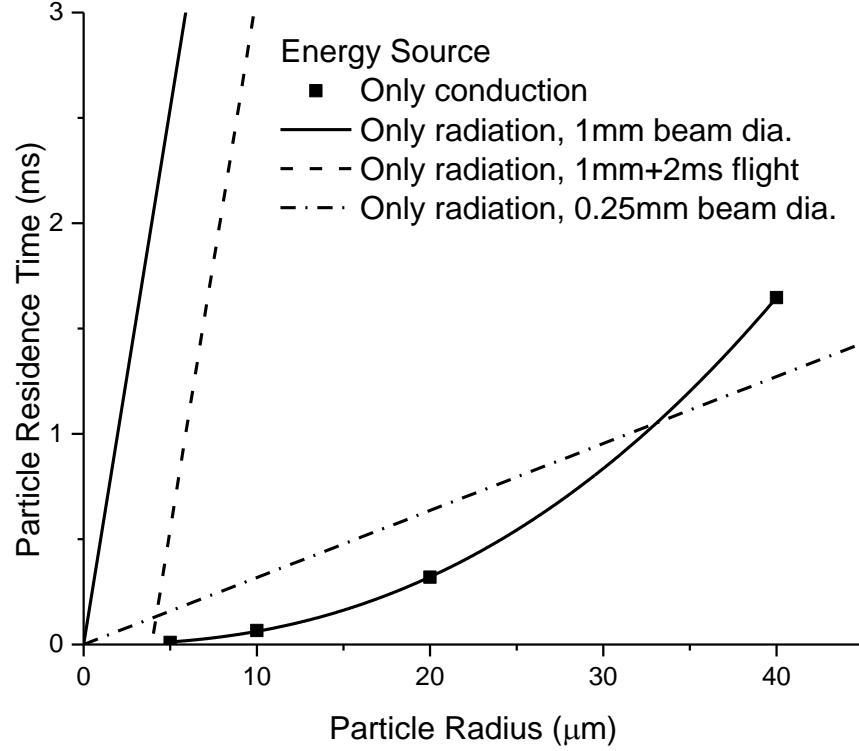


Figure 25. Scaling behavior of particle residence times considering various heat sources. Points are numerically simulated results considering only thermal conduction from the melt pool, and plotted lines are from estimates of radiation energy directly from the incident laser to the particle. Energy delivery from the laser depends strongly on intensity and beam diameter, and can compete with conduction.

4.3 Wettability, Momentum, and Particle Motion

As known from previous literature studying isothermal PMMA particle impacts onto water, particle behavior depends strongly on the wettability and surface properties of the particle and the liquid. Particles can either be trapped by surface tension and oscillate, rebound off the surface, or above a certain critical velocity, penetrate into the bulk of the fluid [69], leaving a vapor cavity behind them which collapses in various ways [66]. In each case, there is a competition between the initial kinetic energy of the particle and the work done to wet and submerge the particle, as reviewed in Section 1.2. These scenarios are in fact reproduced by the medium fidelity model when the surface energies are modified to change the contact angle, as shown in Figure 26:

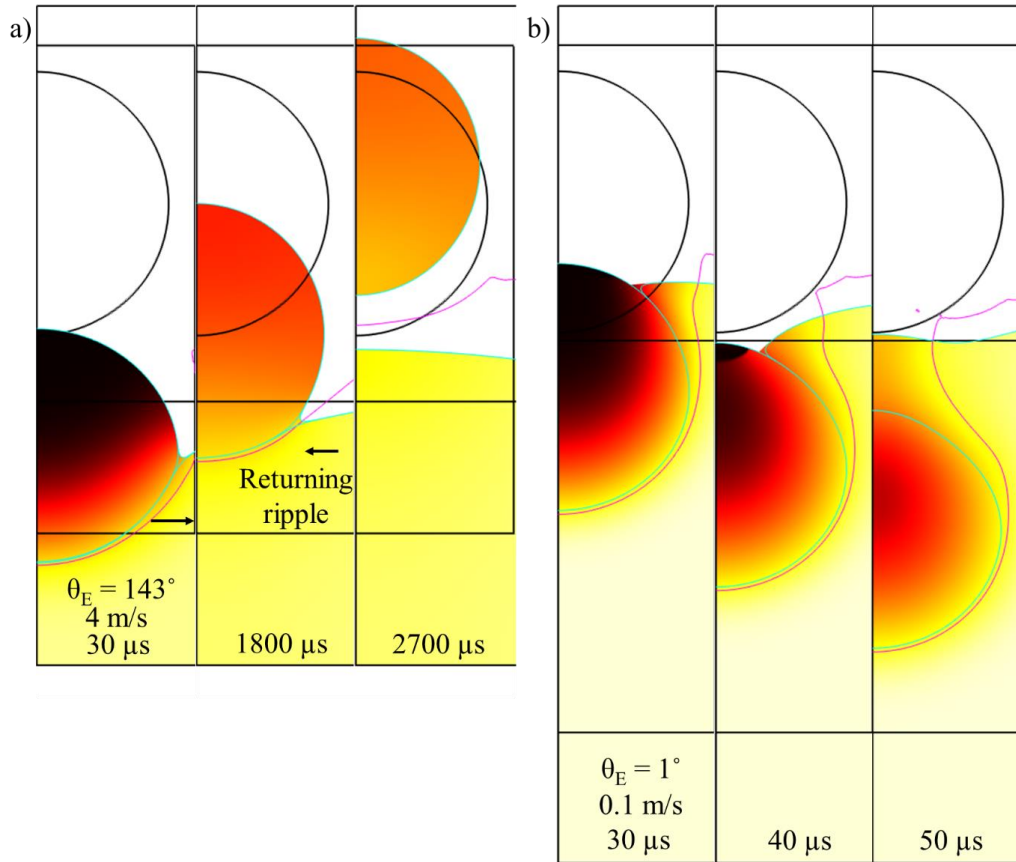


Figure 26. Low and high wettability particles that demonstrate different behavioral regimes; in a) the particle is not energetically strongly bound to the melt pool by surface tension, so a ripple returning from the perimeter from the simulation domain is able to cast it upward and off of the melt pool. In b) the particle wets so well that the energy threshold barrier to penetrating into the fluid bulk has disappeared; even with a very low initial velocity of 0.1 m/s it is drawn into the melt rapidly. This is quite different than the oscillation behavior observed in Figure 21 where the particle is stopped by surface tension and subsequently follows the movement of the melt surface.

It is worth noting that the three-phase field formulation is an energy minimization routine which moves toward the equilibrium contact angle θ_E established by the surface energies between the three phases ($\sigma_{SL}, \sigma_{SV}, \sigma_{LV}$). As such, it is not capable of expressing different values for the advancing and retreating contact angles, so the particle is effectively perfectly smooth. Surface roughness tends to be on the order of the solidification dendrites that form during gas atomization, of 1-5 μm for the present system. The diffuse phase field model cannot resolve this currently without significant improvements in mesh density and increasing computation time drastically.

Neglecting receding angles directly modifies Eqn (23)-(25) and the threshold velocities for particle submergence, rebound, and oscillation. Disparate advancing and retreating angles allows for a greater degree of work to be done removing the particle from the melt surface, which implies that real particles with rough surfaces can be expected to be less prone to ejection from the melt pool surface.

As stated in Section 1.3, determining quantitative values for contact angles have many practical problems, as contact depends strongly on temperature, concentration of surface and alloying elements, surface roughness, and the accuracy of the method chosen to measure these effects. Eustathopoulos lists energies for 66 liquid elements, and classifies 29 of them as having ‘class A’ accuracy, where error is less than $\pm 5\%$ and the temperature dependence coefficient of surface tension is better than $\pm 50\%$; and for 37 elements as ‘class B’ which have accuracy worse than this. This is for liquid-vapor surface tensions, which are the best understood of the three relevant values (σ_{SL} , σ_{SV} , σ_{LV}), and for pure elemental systems without complicating the issue with alloying, surface active elements or oxide formation. Therefore, this study chose to simulate a range of different contact angles to attempt to understand the sensitivity and different behavioral regimes possible. The surface residence times for the chosen contact angle values are contained in Figure 23 d).

Despite the challenges in obtaining a reasonable value for contact angles and particle wettability evident from the literature, the clear dependence of thermal transfer on the particle wettability in Figure 23 d) demonstrates that it is critically important for the accurate estimation of residence time. While other studies have been able to measure contact angle of micron-scale particles on water using high speed video, the optical opacity prevents similar goniometric methods for metal systems. However, two imperfect measurement methods are readily available,

which help to establish some bounded expectations for stainless steel 316L particles. As shown in Figure 27 where high speed images illuminated vertically from the top, described in prior publications [10], the distance between the reflection off the top of the particle and the reflection off of the meniscus gives a relative sense of how ‘high’ the particle is sitting out of the melt relative to its diameter. Images imply a fairly large contact angle/low wettability – perhaps larger than 135° , but very likely greater than 90° . Second, after solidification many particles are frozen in place before fully melting, allowing for metallographic cross sections for contact angle estimates. This is a weak estimate for several reasons including that as the particles may not have been sectioned through the center of the particle, leading to potentially underestimating the contact angle. Additionally, the solidification would be associated with some volume change which would adjust the apparent frozen position of the meniscus.

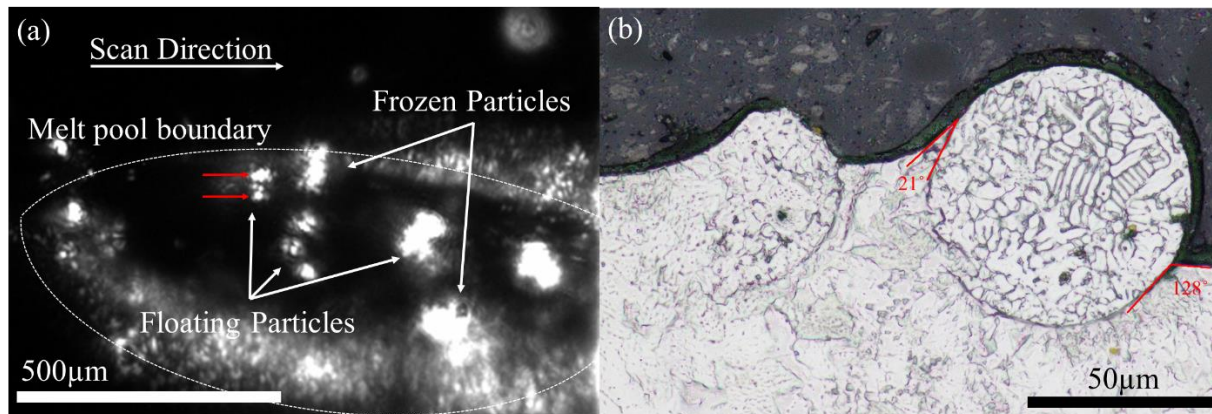


Figure 27. High speed video a) and metallography b) for estimating particle-melt contact angles.

Red arrows highlight laser reflections off the top of the particle and the meniscus, as this is roughly the diameter of the particle it can be understood to be mostly not wetted and ‘ferrophobic’ ($\theta_E > 90^\circ$). Metallography shows highly disparate contact angles (21° and 128°) on the same particle, indicative of highly dynamic behavior.

Interestingly, the measured particle has two very different contact angles on either side of the cross section. This was observed on a number of different particles at a wide variety of conditions in single track experiments. This could potentially be due to the disparity between

advancing and retreating angles on the particle, or perhaps is due to the dynamic dissolution of the oxide layer, or perhaps is just an artifact of how the melt pool solidifies beneath it. While the reasons for this observation are currently unproven, it does demonstrate that a wide range of contact angles are possible in a real system, and that further study is warranted.

While specific predictions for wettability of metallic particles remains highly challenging, the trends observed suggest a wealth of new research avenues for improving the L-DED process. Long particle residence times on the melt pool surface can be understood to contribute to surface roughness and loss of mass capture efficiency [10], so minimizing this period may improve the efficiency of the system and quality of the produced parts. Many surface treatments for powders exist that would modify their ‘ferrophobicity’. Oxides might be removed in hydrogen rich atmospheres or plasma treatments, or systematically added and structured through heating in a controlled oxygen containing atmosphere in a fluidized bed reactor. Powders can be coated with thin layers of other alloys that may not modify the bulk chemistry of the deposit significantly, but improve the particle wetting. Surface roughness and morphology of other powder production methods can be extremely different from the commonly used gas atomized powders; water atomization produces more irregular powders (and a different oxide structure), while Plasma Rotating Electrode Powders (PREP) have gained popularity in the AM field for being highly smooth, spherical, and of low size dispersion. Gas atomized powders are known to have many ‘satellite’ particles of smaller diameter attached to them, which would alter the shape of the meniscus and make wetting more energetically difficult. The surface tension and surface tension temperature dependence coefficient of the fluid can be modified through systemic doping with surface active elements or through better control of trace impurity elements, although these tend to produce lower surface tensions (and lower equilibrium contact angles). Many studies in the AM

literature already incorporate some of these options as study variables, but have not considered powder particle wettability as a controlling factor. The presented model identifies, but is far from completely filling, a completely unaddressed gap in the understanding of the L-DED AM process.

Summary

As powder particles impact the melt pool, they are strongly acted on by surface tension forces which trap them at the melt surface for a brief residence time before they fully melt. To better understand this, a series of numerical models were constructed that tracked the solid, liquid, and gas phase boundaries and heat and mass flow from the time of impact through full melting. These models revealed the scaling influences of particle and melt pool temperature, material properties, impact velocity, and surface tension. These influences can be reasonably estimated with a direct analytical solution for spherical heat conduction away from a point heat sink. This captures particle residence time as a function of material properties, powder morphology, and machine parameters needing only one empirically determined prefactor term to account for particle wettability. Numerical and analytical predictions for heat conduction can be compared to an estimation of incident laser energy delivered directly to the particle allowing comparison of dominant heat transport mechanisms.

While mathematically simple, these estimations provide a powerful, physically significant tool to describe the interactions observed in prior high speed video experiments and may provide information for further, more computationally expensive numerical models. It is the goal of future work to use these estimates to map particle trajectories and lifetimes in a melt pool scale model considering particle-fluid interactions and the more complicated convective flows induced by thermocapillary convection and other sources.

FUTURE WORK

Many open avenues of inquiry remain despite what has been learned about Laser Directed Energy Deposition (L-DED) through the course of this work and the rapid progress of the AM field. As emphasized through this dissertation, the L-DED system incorporates many physical phenomena that happen on highly disparate time and length scales, which complicates simulations and in-situ measurement efforts. In Chapter One a hierarchical simulation discovered a coupling between the powder spray pattern and the dimension evolution of the whole build, which predicted a natural feedback loop in working distance. While interesting and useful, further degrees of coupling could be explored through simulation in other aspects of L-DED; for instance:

- The laser focus and intensity changes with working distance, which could change the thermal distribution in the melt pool and alter the long term stable working distance. This influence could be captured through further improvements of the existing MATLAB model and replicated experimentally.
- In Chapter one, the simplified melt pool model used ignored many shape effects including the topology of the underlying support material. These shaping effects could influence the passive stability point and other large scale behaviors. These effects might be elucidated through incorporating a more rigorous Computational Fluid Dynamics (CFD) melt pool model to a larger scale whole part model.
- Particle impact on the melt pool imposes a highly local thermal sink and momentum and mass source which are typically averaged or ignored in melt pool fluid flow models. Given that impact vectors are not fully stochastic, but instead depend on spray trajectories from the nozzle, an unexplored relationship may exist between particle wetting, spray pattern, and melt pool shape. While resolving individual particles on a melt pool scale model may be

computationally achievable with high performance computing clusters, it is possible that behaviors captured by a high resolution local particle impact model could be packaged into a coupled Discrete Element Method (DEM)/CFD schema to observe this coupling.

These efforts to improve cross-scale coupling in models may reveal new insights about systematic dependencies in L-DED. This permits optimization of machine design to account and compensate for the discovered behaviors, and generate forward progress in the viability of the L-DED technique.

SUMMARY OF THE DISSERTATION

The Laser Directed Energy Deposition (L-DED) process has become an established method for industrial Additive Manufacturing and has attracted many scientific studies focused on dissecting various relevant physical phenomena and effective methods for control. However, several critical gaps in the current understanding of L-DED exist due to the high range of time and length scales over which the process occurs, which limit both in-situ monitoring methods and numerical modelling techniques. In the first chapter, a previously unquantified long-time scale, multilayer feedback loop between the powder spray pattern and the working distance was identified and modelled. In the second chapter, a short time scale phenomenon was observed with high speed video where individual powder particles were found to be trapped for a period of tens to hundreds of microseconds by surface tension on the melt pool surface before finally melting. While short lived, the cumulative effect of this particle residence demonstrably reduces mass capture efficiency and results in final deposit surface roughness. In the third chapter, the contributing factors governing this residence time are numerically modelled with a three-phase CFD model that tracks thermal flow and melting of an individual powder particle. Parameter sensitivity of the numerical results are condensed into an analytical formula useful for first order approximations of powder residence times in diverse material and machine systems. These three chapters demonstrate that the mass capture mechanisms present in L-DED fundamentally alter the macro- and micro-scale behavior at both long and short time scales, and that a mechanistic understanding of these effects should be considered in process control method development.

REFERENCES

- [1] D. D. Gu, W. Meiners, K. Wissenbach, and R. Poprawe, "Laser additive manufacturing of metallic components: materials, processes and mechanisms," *Int. Mater. Rev.*, vol. 57, no. 3, pp. 133–164, May 2012.
- [2] H. Bikas, P. Stavropoulos, and G. Chryssolouris, "Additive manufacturing methods and modelling approaches: a critical review," *Int. J. Adv. Manuf. Technol.*, vol. 83, no. 1–4, pp. 389–405, Mar. 2016.
- [3] P. M. Sammons, D. A. Bristow, and R. G. Landers, "Height Dependent Laser Metal Deposition Process Modeling," *J. Manuf. Sci. Eng.-Trans. ASME*, vol. 135, no. 5, p. 054501, Oct. 2013.
- [4] Y. S. Lee and D. F. Farson, "Surface tension-powered build dimension control in laser additive manufacturing process," *Int. J. Adv. Manuf. Technol.*, vol. 85, no. 5–8, pp. 1035–1044, Jul. 2016.
- [5] Y. Wang, Q. Shi, and H. L. Tsai, "Modeling of the effects of surface-active elements on flow patterns and weld penetration," *Metall. Mater. Trans. B-Proc. Metall. Mater. Proc. Sci.*, vol. 32, no. 1, pp. 145–161, Feb. 2001.
- [6] Z. Li, K. Mukai, M. Zeze, and K. C. Mills, "Determination of the surface tension of liquid stainless steel," *J. Mater. Sci.*, vol. 40, no. 9–10, pp. 2191–2195, May 2005.
- [7] W. E. King *et al.*, "Observation of keyhole-mode laser melting in laser powder-bed fusion additive manufacturing," *J. Mater. Process. Technol.*, vol. 214, no. 12, pp. 2915–2925, Dec. 2014.
- [8] M. Courtois, M. Carin, P. Le Masson, S. Gaied, and M. Balabane, "A new approach to compute multi-reflections of laser beam in a keyhole for heat transfer and fluid flow modelling in laser welding," *J. Phys. D-Appl. Phys.*, vol. 46, no. 50, p. 505305, Dec. 2013.
- [9] W. I. Cho, S. J. Na, C. Thomy, and F. Vollertsen, "Numerical simulation of molten pool dynamics in high power disk laser welding," *J. Mater. Process. Technol.*, vol. 212, no. 1, pp. 262–275, Jan. 2012.
- [10] J. C. Haley, J. M. Schoenung, and E. J. Lavernia, "Observations of particle-melt pool impact events in directed energy deposition," *Additive Manufacturing*, vol. 22, pp. 368–374, Aug. 2018.
- [11] K. Shah, A. J. Pinkerton, A. Salman, and L. Li, "Effects of Melt Pool Variables and Process Parameters in Laser Direct Metal Deposition of Aerospace Alloys," *Mater. Manuf. Process.*, vol. 25, no. 12, pp. 1372–1380, 2010.
- [12] W. Hofmeister and M. Griffith, "Solidification in direct metal deposition by LENS processing," *JOM*, vol. 53, pp. 30–34.
- [13] U. S. Bertoli, G. Guss, S. Wu, M. J. Matthews, and J. M. Schoenung, "In-situ characterization of laser-powder interaction and cooling rates through high-speed imaging of powder bed fusion additive manufacturing," *Mater. Des.*, vol. 135, pp. 385–396, Dec. 2017.
- [14] M. J. Matthews, G. Guss, S. A. Khairallah, A. M. Rubenchik, P. J. Depond, and W. E. King, "Denudation of metal powder layers in laser powder bed fusion processes," *Acta Mater.*, vol. 114, pp. 33–42, Aug. 2016.
- [15] S. K. Everton, M. Hirsch, P. Stravroulakis, R. K. Leach, and A. T. Clare, "Review of in-situ process monitoring and in-situ metrology for metal additive manufacturing," *Mater. Des.*, vol. 95, pp. 431–445, Apr. 2016.

- [16] M. Doubenskaia, P. Bertrand, and I. Smurov, "Optical monitoring of Nd: YAG laser cladding," *Thin Solid Films*, vol. 453, pp. 477–485, Apr. 2004.
- [17] Q. Wang, J. Li, M. Gouge, A. R. Nassar, P. Michaleris, and E. W. Reutzel, "Physics-Based Multivariable Modeling and Feedback Linearization Control of Melt-Pool Geometry and Temperature in Directed Energy Deposition," *J. Manuf. Sci. Eng.-Trans. ASME*, vol. 139, no. 2, p. 021013, Feb. 2017.
- [18] A. J. Pinkerton, "Advances in the modeling of laser direct metal deposition," *J. Laser Appl.*, vol. 27, p. 7, Feb. 2015.
- [19] P. Michaleris, "Modeling metal deposition in heat transfer analyses of additive manufacturing processes," *Finite Elem. Anal. Des.*, vol. 86, pp. 51–60, Sep. 2014.
- [20] L. Wang, X. Jiang, Y. Zhu, X. Zhu, J. Sun, and B. Yan, "An approach to predict the residual stress and distortion during the selective laser melting of AlSi10Mg parts," *Int J Adv Manuf Technol*, vol. 97, no. 9–12, pp. 3535–3546, Aug. 2018.
- [21] P. Peyre, P. Aubry, R. Fabbro, R. Neveu, and A. Longuet, "Analytical and numerical modelling of the direct metal deposition laser process," *J. Phys. D-Appl. Phys.*, vol. 41, no. 2, p. 025403, Jan. 2008.
- [22] P. Balu, P. Leggett, and R. Kovacevic, "Parametric study on a coaxial multi-material powder flow in laser-based powder deposition process," *J. Mater. Process. Technol.*, vol. 212, no. 7, pp. 1598–1610, Jul. 2012.
- [23] J. A. Koepf, M. R. Gotterbarm, M. Markl, and C. Körner, "3D multi-layer grain structure simulation of powder bed fusion additive manufacturing," *Acta Materialia*, vol. 152, pp. 119–126, Jun. 2018.
- [24] S. Geng *et al.*, "Cellular automaton modeling for dendritic growth during laser beam welding solidification process," *Journal of Laser Applications*, vol. 30, no. 3, p. 032406, Jun. 2018.
- [25] V. D. Manvatkar, A. A. Gokhale, G. J. Reddy, A. Venkataramana, and A. De, "Estimation of Melt Pool Dimensions, Thermal Cycle, and Hardness Distribution in the Laser-Engineered Net Shaping Process of Austenitic Stainless Steel," *Metall. Mater. Trans. A-Phys. Metall. Mater. Sci.*, vol. 42A, no. 13, pp. 4080–4087, Dec. 2011.
- [26] G. Tapia and A. Elwany, "A Review on Process Monitoring and Control in Metal-Based Additive Manufacturing," *J. Manuf. Sci. Eng.-Trans. ASME*, vol. 136, no. 6, p. 10, Dec. 2014.
- [27] D. Wang, C. Song, Y. Yang, and Y. Bai, "Investigation of crystal growth mechanism during selective laser melting and mechanical property characterization of 316L stainless steel parts," *Mater. Des.*, vol. 100, pp. 291–299, Jun. 2016.
- [28] Y. H. Xiong, J. E. Smugeresky, and J. M. Schoenung, "The influence of working distance on laser deposited WC-Co," *J. Mater. Process. Technol.*, vol. 209, no. 10, pp. 4935–4941, Jun. 2009.
- [29] G. A. Turichin *et al.*, "Technological aspects of high speed direct laser deposition based on heterophase powder metallurgy," in *15th Nordic Laser Materials Processing Conference, NOLAMP 15*, vol. 78, A. Salminen, Ed. Amsterdam: Elsevier Science Bv, 2015, pp. 397–406.
- [30] C. Knapp, T. Lienert, J. Carpenter, and D. Kovar, "In Situ Monitoring of Directed Energy Deposition," presented at the MS&T, Salt Lake City, Utah, 2016.
- [31] P. Balu, P. Leggett, S. Hamid, and R. Kovacevic, "Multi-Response Optimization of Laser-based Powder Deposition of Multi-track Single Layer Hastelloy C-276," *Mater. Manuf. Process.*, vol. 28, no. 2, pp. 173–182, Feb. 2013.

- [32] S. Kumar, V. Sharma, A. K. S. Choudhary, S. Chattopadhyaya, and S. Hloch, "Determination of layer thickness in direct metal deposition using dimensional analysis," *Int. J. Adv. Manuf. Technol.*, vol. 67, no. 9–12, pp. 2681–2687, Aug. 2013.
- [33] Y. Sun and M. Hao, "Statistical analysis and optimization of process parameters in Ti6Al4V laser cladding using Nd:YAG laser," *Opt. Lasers Eng.*, vol. 50, no. 7, pp. 985–995, Jul. 2012.
- [34] U. de Oliveira, V. Ocelik, and J. T. M. De Hosson, "Analysis of coaxial laser cladding processing conditions," *Surf. Coat. Technol.*, vol. 197, no. 2–3, pp. 127–136, Jul. 2005.
- [35] D. Rosenthal, *The theory of moving sources of heat and its application to metal treatments*. Cambridge: ASME, 1946.
- [36] J. Beuth and N. Klingbeil, "The role of process variables in laser-based direct metal solid freeform fabrication," *JOM-J. Miner. Met. Mater. Soc.*, vol. 53, no. 9, pp. 36–39, Sep. 2001.
- [37] J. Gockel, N. Klingbeil, and S. Bontha, "A Closed-Form Solution for the Effect of Free Edges on Melt Pool Geometry and Solidification Microstructure in Additive Manufacturing of Thin-Wall Geometries," *Metall. Mater. Trans. B-Proc. Metall. Mater. Proc. Sci.*, vol. 47, no. 2, pp. 1400–1408, Apr. 2016.
- [38] B. Zheng, Y. Zhou, J. E. Smugeresky, J. M. Schoenung, and E. J. Lavernia, "Thermal Behavior and Microstructural Evolution during Laser Deposition with Laser-Engineered Net Shaping: Part I. Numerical Calculations," *Metallurgical and Materials Transactions A*, vol. 39, pp. 2228–2236, Sep. 2008.
- [39] V. Manvatkar, A. De, and T. DebRoy, "Heat transfer and material flow during laser assisted multi-layer additive manufacturing," *J. Appl. Phys.*, vol. 116, no. 12, p. 124905, Sep. 2014.
- [40] P. Schweitzer, *Metallic Materials: Physical, Mechanical, and Corrosion Properties*. New York: Marcel Dekker, 2003.
- [41] R. BOGAARD, P. DESAI, H. LI, and C. HO, "THERMOPHYSICAL PROPERTIES OF STAINLESS-STEELS," *Thermochim. Acta*, vol. 218, pp. 373–393, May 1993.
- [42] M. Baucio, *ASM Metals Reference Book, 3rd Edition*. ASM International, 1993.
- [43] K. C. Mills, *Recommended Values of Thermophysical Properties for Selected Commercial Alloys*. Cambridge: Woodhead, 2002.
- [44] S. Krishnan, K. J. Yugawa, and P. C. Nordine, "Optical properties of liquid nickel and iron," *Phys. Rev. B*, vol. 55, no. 13, pp. 8201–8206, Apr. 1997.
- [45] D. Meschede, *Optics, Light, and Lasers: The Practical Approach to Modern Aspects of Photonics and Laser Physics*. Weinheim, Germany: Wiley-VCH Verlag GmbH & Co. KGaA, 2017.
- [46] W. Devesse, D. De Baere, and P. Guillaume, "The isotherm migration method in spherical coordinates with a moving heat source," *Int. J. Heat Mass Transf.*, vol. 75, pp. 726–735, Aug. 2014.
- [47] N. Chakraborty, "Thermal transport regimes and effects of prandtl number in molten pool transport in laser surface melting processes," *Numer. Heat Transf. A-Appl.*, vol. 53, no. 3, pp. 273–294, 2008.
- [48] H. El Cheikh, B. Courant, J.-Y. Hascoet, and R. Guillen, "Prediction and analytical description of the single laser track geometry in direct laser fabrication from process parameters and energy balance reasoning," *J. Mater. Process. Technol.*, vol. 212, no. 9, pp. 1832–1839, Sep. 2012.
- [49] J. J. Lewandowski and M. Seifi, "Metal Additive Manufacturing: A Review of Mechanical Properties," in *Annual Review of Materials Research, Vol 46*, vol. 46, D. R. Clarke, Ed. Palo Alto: Annual Reviews, 2016, pp. 151–186.

- [50] J. M. Drezet, S. Pellerin, C. Bezencon, and S. Mokadem, "Modelling the Marangoni convection in laser heat treatment," *J. Phys. IV*, vol. 120, pp. 299–306, Dec. 2004.
- [51] O. B. Kovalev, A. V. Zaitsev, D. Novichenko, and I. Smurov, "Theoretical and Experimental Investigation of Gas Flows, Powder Transport and Heating in Coaxial Laser Direct Metal Deposition (DMD) Process," *J. Therm. Spray Technol.*, vol. 20, no. 3, pp. 465–478, Mar. 2011.
- [52] S. Zekovic, R. Dwivedi, and R. Kovacevic, "Numerical simulation and experimental investigation of gas-powder flow from radially symmetrical nozzles in laser-based direct metal deposition," *Int. J. Mach. Tools Manuf.*, vol. 47, no. 1, pp. 112–123, Jan. 2007.
- [53] Y. H. Xiong, W. H. Hofmeister, J. E. Smugeresky, J. P. Delplanque, and J. M. Schoenung, "Investigation of atypical molten pool dynamics in tungsten carbide-cobalt during laser deposition using in-situ thermal imaging," *Appl. Phys. Lett.*, vol. 100, no. 3, p. 4, Jan. 2012.
- [54] D. A. Kriczky, J. Irwin, E. W. Reutzel, P. Michaleris, A. R. Nassar, and J. Craig, "3D spatial reconstruction of thermal characteristics in directed energy deposition through optical thermal imaging," *J. Mater. Process. Technol.*, vol. 221, pp. 172–186, Jul. 2015.
- [55] F. Mazzucato, S. Tusacciu, M. Lai, S. Biamino, M. Lombardi, and A. Valente, "Monitoring Approach to Evaluate the Performances of a New Deposition Nozzle Solution for DED Systems," *Technologies*, vol. 5, no. 2, p. 29, Jun. 2017.
- [56] I. F. Sbalzarini and P. Koumoutsakos, "Feature point tracking and trajectory analysis for video imaging in cell biology," *J. Struct. Biol.*, vol. 151, no. 2, pp. 182–195, Aug. 2005.
- [57] S. Y. Bae, C. H. Jung, and Y. P. Kim, "Derivation and verification of an aerosol dynamics expression for the below-cloud scavenging process using the moment method," *Journal of Aerosol Science*, vol. 41, no. 3, pp. 266–280, Mar. 2010.
- [58] A. Wang, Q. Song, and Q. Yao, "Behavior of hydrophobic micron particles impacting on droplet surface," *Atmos. Environ.*, vol. 115, pp. 1–8, Aug. 2015.
- [59] D. Vella and P. D. Metcalfe, "Surface tension dominated impact," *Phys. Fluids*, vol. 19, no. 7, p. 072108, Jul. 2007.
- [60] J.-L. Liu, X.-Q. Feng, and G.-F. Wang, "Buoyant force and sinking conditions of a hydrophobic thin rod floating on water," *Phys. Rev. E*, vol. 76, no. 6, p. 066103, Dec. 2007.
- [61] A. M. Worthington, "Impact with a liquid surface studied by the aid of instantaneous photography. Paper II.," *Philos. Trans. R. Soc. Lond. A-Contain. Pap. Math. Phys. Character*, vol. 194, pp. 175-U36, 1900.
- [62] C. Duez, C. Ybert, C. Clanet, and L. Bocquet, "Making a splash with water repellency," *Nat. Phys.*, vol. 3, no. 3, pp. 180–183, Mar. 2007.
- [63] M. Do-Quang and G. Amberg, "The splash of a solid sphere impacting on a liquid surface: Numerical simulation of the influence of wetting," *Phys. Fluids*, vol. 21, no. 2, p. 022102, Feb. 2009.
- [64] M. Do-Quang and G. Amberg, "Numerical simulation of the coupling problems of a solid sphere impacting on a liquid free surface," *Math. Comput. Simul.*, vol. 80, no. 8, pp. 1664–1673, Apr. 2010.
- [65] D.-G. Lee and H.-Y. Kim, "Impact of a superhydrophobic sphere onto water," *Langmuir*, vol. 24, no. 1, pp. 142–145, Jan. 2008.
- [66] J. M. Aristoff and J. W. M. Bush, "Water entry of small hydrophobic spheres," *J. Fluid Mech.*, vol. 619, pp. 45–78, Jan. 2009.
- [67] D. Liu, Q. He, and G. M. Evans, "Penetration behaviour of individual hydrophilic particle at a gas-liquid interface," *Adv. Powder Technol.*, vol. 21, no. 4, pp. 401–411, Jul. 2010.

- [68] D.-G. Lee and H.-Y. Kim, “Sinking of small sphere at low Reynolds number through interface,” *Phys. Fluids*, vol. 23, no. 7, p. 072104, Jul. 2011.
- [69] A. Wang, Q. Song, B. Ji, and Q. Yao, “In-situ observation of hydrophobic micron particle impaction on liquid surface,” *Powder Technol.*, vol. 311, pp. 408–415, Apr. 2017.
- [70] D. M. Kintea, J. Breitenbach, V. T. Gurumurthy, I. V. Roisman, and C. Tropea, “On the influence of surface tension during the impact of particles on a liquid-gaseous interface,” *Phys. Fluids*, vol. 28, no. 1, p. 012108, Jan. 2016.
- [71] B. Ji, Q. Song, and Q. Yao, “Numerical study of hydrophobic micron particle’s impaction on liquid surface,” *Phys. Fluids*, vol. 29, no. 7, p. 077102, Jul. 2017.
- [72] T. Dubberstein, H.-P. Heller, J. Klostermann, R. Schwarze, and J. Brillo, “Surface tension and density data for Fe–Cr–Mo, Fe–Cr–Ni, and Fe–Cr–Mn–Ni steels,” *J Mater Sci*, vol. 50, no. 22, pp. 7227–7237, Nov. 2015.
- [73] L. Xuyang, L. Xuewei, L. Chunxin, C. Jie, and B. Chenguang, “Surface Tension of Liquid Ti–Al Alloys,” *Rare Metal Materials and Engineering*, p. 6, 2017.
- [74] P. Sahoo, T. Debroy, and M. McNallan, “Surface tension of binary metal surface active solute systems under conditions relevant to welding metallurgy,” *Metallurgical Transactions B-Process Metallurgy*, vol. 19, no. 3, pp. 483–491, Jun. 1988.
- [75] S. Schönecker, X. Li, B. Johansson, S. K. Kwon, and L. Vitos, “Thermal surface free energy and stress of iron,” *Scientific Reports*, vol. 5, p. 14860, Oct. 2015.
- [76] N. Eustathopoulos, “Wetting by Liquid Metals-Application in Materials Processing: The Contribution of the Grenoble Group,” *Metals*, vol. 5, no. 1, pp. 350–370, Mar. 2015.
- [77] R. W. Johnson, Ed., *Handbook of Fluid Dynamics, 2nd Edition*. Boca Raton: Crc Press-Taylor & Francis Group, 2016.
- [78] W. F. Gale and T. C. Totemeier, Eds., “14 - General physical properties,” in *Smithells Metals Reference Book (Eighth Edition)*, Oxford: Butterworth-Heinemann, 2004, pp. 14–1.
- [79] P. Yue, C. Zhou, and J. J. Feng, “Spontaneous shrinkage of drops and mass conservation in phase-field simulations,” *Journal of Computational Physics*, vol. 223, no. 1, pp. 1–9, Apr. 2007.
- [80] K. A. Jackson, *Kinetic Processes: Crystal Growth, Diffusion, and Phase Transitions in Materials*. 2005.